HAL
open science

Modeling Immiscible Two-Phase Flow in Rough Fractures From Capillary to Viscous Fingering

Zhibing Yang, Yves Méheust, Insa Neuweiler, Ran Hu, Auli Niemi, Yi-feng Chen

To cite this version:

Zhibing Yang, Yves Méheust, Insa Neuweiler, Ran Hu, Auli Niemi, et al.. Modeling Immiscible Two-Phase Flow in Rough Fractures From Capillary to Viscous Fingering. Water Resources Research, 2019, 55 (3), pp.2033-2056. 10.1029/2018WR024045 . insu-02078662

HAL Id: insu-02078662

https://insu.hal.science/insu-02078662v1

Submitted on 25 Mar 2019

HAL is a multi-disciplinary open access archive for the deposit and dissemination of scientific research documents, whether they are published or not. The documents may come from teaching and research institutions in France or abroad, or from public or private research centers.

L'archive ouverte pluridisciplinaire **HAL**, est destinée au dépôt et à la diffusion de documents scientifiques de niveau recherche, publiés ou non, émanant des établissements d'enseignement et de recherche français ou étrangers, des laboratoires publics ou privés.

Water Resources Research

RESEARCH ARTICLE
10.1029/2018WR024045

Modeling Immiscible Two-Phase Flow in Rough Fractures From Capillary to Viscous Fingering

Zhibing Yang[1], Yves Méheust[2], Insa Neuweiler[3], Ran Hu[1], Auli Niemi[4], and Yi-Feng Chen[1]

[1]State Key Laboratory of Water Resources and Hydropower Engineering Science, Wuhan University, Wuhan, China, [2]Université de Rennes 1, CNRS, Géosciences Rennes (UMR 6118), Rennes, France, [3]Institute of Fluid Mechanics and Environmental Physics in Civil Engineering, Leibniz University Hannover, Germany, [4]Department of Earth Sciences, Uppsala University, Uppsala, Sweden

Key Points:
- An efficient, intermediate-scale model is developed for dynamic, immiscible displacement in rough geological fractures
- The model reproduces essential features of experimentally observed drainage patterns from capillary to viscous fingering
- The model is advantageous over CFD approaches in computational efficiency and accuracy, especially in low to medium capillary number flows

Supporting Information:
- Supporting Information S1
- Data Set S1

Correspondence to:
Z. Yang and Y.-F. Chen,
zbyang@whu.edu.cn;
csyfchen@whu.edu.cn

Citation:
Yang, Z., Méheust, Y., Neuweiler, I., Hu, R., Niemi, A., & Chen, Y.-F. (2019). Modeling immiscible two-phase flow in rough fractures from capillary to viscous fingering. *Water Resources Research*, *55*. https://doi.org/10.1029/2018WR024045

Received 5 SEP 2018
Accepted 18 FEB 2019
Accepted article online 25 FEB 2019

©2019. American Geophysical Union. All Rights Reserved.

Abstract We develop an efficient computational model for simulating fluid invasion patterns emerging in variable aperture fractures. This two-dimensional model takes into account the effect of capillary force on the fluid-fluid interfaces and viscous pressure drop in both fluid phases. The pressure distribution is solved at each time step based on mass balance and local cubic law, considering an imposed pressure jump condition at the fluid-fluid interface. This pressure jump corresponds to the Laplace pressure which includes both terms related to the out-of-plane (aperture-spanning) curvature and to the in-plane curvature. Simulating a configuration that emulates viscous fingering in two-dimensional random porous media confirms that the model accounts properly for the role of viscous forces. Furthermore, direct comparison with previously obtained experimental results shows that the model reproduces the observed drainage patterns in a rough fracture reasonably well. The evolutions of tip location, the inlet pressures, and the invading phase fractal dimensions are analyzed to characterize the transition from capillary fingering to viscous fingering regimes. A radial injection scenario of immiscible invasion is also studied with varying modified capillary number and viscosity ratio, showing displacement patterns ranging from capillary fingering to viscous fingering to stable displacement. Such simulations using two contact angles show that the invading phase becomes more compact when the wetting condition changes from strong to weak drainage, as already observed in 2-D porous media. The model can be used to bridge the gap in spatial scales of two-phase flow between pore-scale modeling approaches and the continuum Darcy-scale models.

Plain Language Summary The flow of two or more fluids in fractured media is an important process involved in many industrial and environmental applications in the subsurface with examples spanning from contaminant transport to petroleum recovery to geological storage of carbon dioxide. Understanding and controlling two-phase flow in fractures is critical from both the scientific and technological points of view. In this study, we focus on the displacement of one fluid by another immiscible one in a rough fracture, a fundamental process underlying two-phase flow in fractured media. We develop an efficient computational model for simulating fluid invasion patterns emerging in rough fractures. This model takes into account the effect of capillary force on the fluid-fluid interfaces and viscous pressure drop in both fluid phases. Direct comparison with experimental results shows that the model output matches the observed patterns reasonably well. In addition, generic simulations demonstrate the ability of the model to produce flow patterns that fall into regimes whose dependence on the viscosity ratio and capillary number is similar to that of the classical phase diagram. The model can be used to bridge the gap in spatial scales of two-phase flow between pore-scale modeling approaches and the continuum Darcy-scale models.

1. Introduction

The flow of two or more fluids in fractured media is an important process involved in many industrial and environmental applications in the subsurface with examples spanning from contaminant transport to petroleum recovery and from geological storage of CO_2 to geothermal energy exploitation. In unconventional reservoirs, two-phase flow in hydraulic fractures plays a key role in the recovery of gas and the flow-back (and the disappearance) of fracturing fluids (Edwards et al., 2017). In groundwater formations, fractured rocks contaminated by nonaqueous phase liquids have been identified as the most difficult cate-

gory of sites for remediation and management (NRC, 2005). In remediation the challenge stems mainly from the large uncertainty in predicting the spatial location and distribution of the contaminant and the difficulty in effectively delivering the remediation agent (Yang, Niemi, Fagerlund, Illangasekare, & Detwiler, 2013; Yeo et al., 2003). In geological sequestration, two-phase flow in fractures arises from potential CO_2 leakage through natural fractures in the caprock initially saturated with brine (Huang et al., 2015). Understanding and controlling two-phase flow in fractures is therefore critical from both the scientific and technological points of view. In this study, we focus on the displacement of one fluid by another immiscible one (immiscible displacement) in a single fracture, a fundamental process underlying two-phase flow in fractured media.

Immiscible two-phase flow in rock fractures is controlled by the interplay between capillary, gravitational, and viscous forces, as well as inertia (Detwiler et al., 2009; Glass et al., 1998; Loggia et al., 2009), as is the case for two-dimensional porous media (Méheust et al., 2002; Toussaint et al., 2012). This interplay is in turn influenced by the wetting condition and the aperture variability associated with fracture wall roughness (Auradou, 2009; Glass et al., 2003; Yang et al., 2016). In the absence of strong gravity effects (e.g., if the fracture plane is horizontal), the flow is controlled by capillary and viscous effects. For porous media, the seminal work of Lenormand et al. (1988) elucidated the mechanisms behind the three observed flow regimes, capillary fingering, viscous fingering, and stable displacement, and presented a phase diagram mapping these three patterns in the Ca–M plane. Here $Ca = \mu_{\mathrm{inv}}V/\gamma$ is the dimensionless capillary number, which characterizes the relative importance of capillary and viscous forces, and $M = \mu_{\mathrm{inv}}/\mu_{\mathrm{def}}$ is the viscosity ratio; μ_{inv} and μ_{def} are the viscosity of the invading and defending phase, respectively; V is the average flow velocity; and γ is the interfacial tension.

Under the influence of gravity/buoyancy, experimental work using water and oil as the fluid-pair has shown that two-phase flow regimes can range from unstable, tortuous fingers and random clusters to stable, piston-like displacement with trapping (Loggia et al., 2009), depending on different combinations of the dimensionless Bond numbers and capillary numbers; the former compares buoyancy to capillary forces and the latter compares viscous to capillary forces. Observations of unsaturated flow in fractures, that is, the much more viscous, denser water, infiltrating and displacing the nonwetting fluid air of small viscosity and negligible density, have revealed a wide range of unstable flow dynamics, including continuous rivulet (Kneafsey & Pruess, 1998), intermittent or snapping rivulets (Su et al., 2001, 2004), film flow (Tokunaga & Wan, 1997), and sliding drops (Kordilla et al., 2017).

For horizontal fractures, a number of experimental studies on two-phase flow have been reported over the past two to three decades (e.g., Amundsen et al., 1999; Arshadi et al., 2018; C.-Y. Chen & Horne, 2006; Y.-F. Chen et al., 2017; Ferer et al., 2011; Fourar et al., 1993; Huo & Benson, 2016; Hu, Wu, et al., 2018; Karpyn & Piri, 2007; Neuweiler et al., 2004; Persoff & Pruess, 1995; Pyrak-Nolte et al., 1992; Reitsma & Kueper, 1994; Watanabe et al., 2015). Many of these studies have focused on pursuing suitable continuum/Darcy-scale descriptions (i.e., capillary pressure and relative permeabililities as a function of saturation) using natural rock fractures (e.g., Arshadi et al., 2018; Huo & Benson, 2016; Reitsma & Kueper, 1994; Watanabe et al., 2015) or their transparent replicas (e.g., Nowamooz et al., 2009; Persoff & Pruess, 1995; Pyrak-Nolte et al., 1992). The obtained capillary pressure and relative permeability relationships are particularly useful when one needs to predict two-phase flow behavior at the field scale, where the fine details at the subfracture scale will be difficult to incorporate. However, since the connectivity and arrangement of phases control how fluids flow (Blunt, 2017), those constitutive relationships are themselves dependent on the fluid phase configuration within a considered volume for averaging. The phase configuration is in turn governed by the interplay between various forces at the microscale. It is thus expected that the flow regimes dictated by the capillary number and viscosity ratio will impact the empirical constitutive relationships or even in some cases impair the construction of these relationships. In order to study the flow regimes under various capillary numbers and viscosity ratios in a geological fracture, Y.-F. Chen et al. (2017) recently carried out a systematic study of the transition from capillary fingering to viscous fingering using visualization of flow experiments in a transparent replica of the fracture. Hu, Wu, et al. (2018) analyzed the energy conversion and dissipation during imbibition in a rough fracture and linked flow regime transition to energy conversion.

Various numerical approaches have been proposed to simulate the flow patterns emerging during immiscible displacement in rough-walled fractures. For quasi-static displacement where capillary forces dominate

viscous forces, the invasion percolation model (Chandler et al., 1982; Wilkinson & Willemsen, 1983) originally proposed for porous media flow has been modified to include the effect of fragmentation (Amundsen et al., 1999) and the effect of the minor principle interfacial curvature, commonly referred to as the in-plane curvature (Glass et al., 1998; Neuweiler et al., 2004; Yang et al., 2012). Due to its smoothening effect, the in-plane curvature has been shown to strongly influence the invasion dynamics (Glass et al., 2003; Yang et al., 2016). Another type of quasi-static model applied to studying immiscible displacement in fracture is the level set method-based progressive quasi-static model (Tokan-Lawal et al., 2015). In the abovementioned quasi-static approaches, the viscous effects are ignored, and thus these models are generally limited to capillary-dominated conditions, corresponding to sufficiently small capillary numbers.

As the flow rate increases, viscous effects become comparable to capillary effects, and the viscous pressure drop must be taken into account in numerical models of immiscible displacement in a fracture. Consequently, the pressure field and the fluid interface displacement have to be solved simultaneously at any time. One common approach consists in modifying the traditional continuum two-phase flow model (based on the continuity equations and Darcy's laws for both phases) to include the fracture geometry and aperture variability as well as the associated aperture-induced capillarity (Murphy & Thomson, 1993; Yang, Niemi, Fagerlund, & Illangasekare, 2013). A disadvantage of this approach is that it cannot account for the effect of the in-plane interface curvature. Another approach is to transform the fracture void space into a pore-network and thus apply dynamic pore-network models to simulate fluid invasion in the fracture (e.g., Ferer et al., 2011; Hughes & Blunt, 2001; Karpyn & Piri, 2007). However, the definition of a pore-network that would be the hydraulic equivalent of a given fracture is not straightforward. In addition, such models lack a realistic inclusion of the effect of in-plane curvature. In recent years, with the ever-increasing computing power and parallelization, a number of studies have resorted to highly resolved first principle modeling of fluid flow and fluid-fluid interface displacement based on, for example, computational fluid dynamics (CFD) simulations with interface capturing/tracking techniques (e.g., Basirat et al., 2017; Y.-F. Chen et al., 2018; Ferrari & Lunati, 2013; Meakin & Tartakovsky, 2009), lattice Boltzmann simulations (e.g., Dou et al., 2013), and smoothed particle hydrodynamics (e.g., Tartakovsky & Meakin, 2005). Despite the advances in these highly resolved subpore-scale simulation methods, in general it remains computationally very expensive, often to the point of being restrictive, to reliably simulate two-phase flow in a variable aperture fracture of a reasonable size, even with parallelization using many cores. For example, a fracture of size 1×1 cm and mean aperture 200 μm already results in 2,500,000 grid cells of size 20 μm. Simulations of two-phase flow in rough-walled fractures of this size (1×1 cm) fall quite short of upscaling purposes. In addition, it is still challenging for CFD techniques to accurately model the immiscible fluid-fluid displacement at the pore scale in capillary driven flows, due to the spurious currents or "parasitic" velocities introduced during the computation of the interface curvature (Y.-F. Chen et al., 2018; Roman et al., 2016). Therefore, there is a strong need to develop efficient, reliable models of immiscible displacement in fractures that can capture the essential physics of the interplay between the different forces and simulate two-phase flow in systems sufficiently large for upscaling purposes.

Successful direct comparison between experimental invasion patterns and patterns obtained from numerical simulations are rarely reported (with notable exceptions, e.g., the study by Ferrari et al., 2015, in 2-D porous media and Y.-F. Chen et al., 2018, in a 3-D rough fracture), specially if they are performed over a wide range of capillary numbers and viscosity ratios. In this study we develop a new computational model capable of predicting fluid-fluid displacement in variable aperture fractures in the full range of viscosity ratios and various wetting angles normally encountered in the subsurface. This two-dimensional (2-D) model accounts for the effect of capillary force on the fluid-fluid interfaces and viscous pressure drop in both phases. One of its main strengths is its computational efficiency, in particular at relatively large capillary numbers for which viscous forces play an important role in controlling the geometry of the invasion pattern. To validate the model, we use recently published experimental observations (Y.-F. Chen et al., 2017). In the following we first describe the model in detail. We then use the model to simulate fluid displacement in a horizontal fracture and confront the results to experimental data (Y.-F. Chen et al., 2017) obtained in the same fracture geometry, under various capillary numbers and viscosity ratios. We also apply the model to simulating immiscible two-phase in a radial injection scenario and analyze the impact of the contact angle on the displacement patterns.

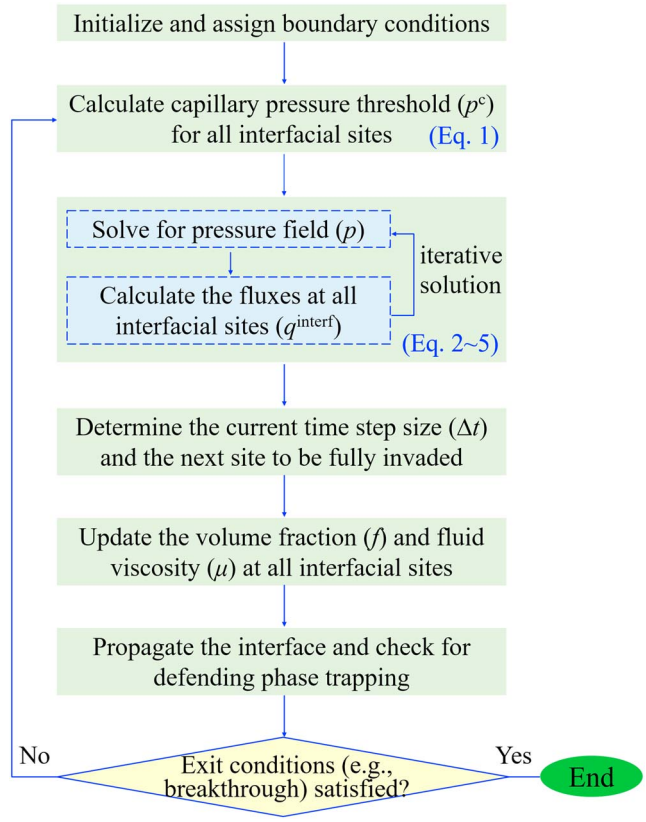

Figure 1. Calculation scheme for modeling the fluid-fluid displacement in a variable aperture fracture. The states of the model are given by pressure p and fluid volume fraction f at each site. The interface is explicitly tracked, and the curvatures (and thus the local capillary pressure) along the interface are calculated. The numerical procedure updates p and f in discrete time steps until a preset exit condition is met.

2. Methods

2.1. Model Development

In this section, we describe the numerical model in detail, including (i) the overall calculation procedure for fluid-fluid displacement (see Figure 1), (ii) the discretization of the space between the fracture walls, (iii) the tracking of fluid-fluid interfaces and the calculation of interfacial curvatures, (iv) the procedure for computing the pressure distribution in the fracture, and the rules of fluid invasion and interface advancement. We are mainly interested in the interplay between the capillary forces and the viscous forces. Gravity and inertia are not considered in the model. Film flows and corner flows are neglected. Contact pinning and hysteresis are not accounted for either.

2.1.1. Representation of a Rough-Walled Fracture

Natural fractures have variable apertures. We represent the space between the fracture walls as an ensemble of parallelepipedic boxes, positioned on a 2-D lattice over the facture plane. The projection on the fracture plane of one of these "local parallel plates" is denoted by *site* in the following. The position of each site is referenced by indices i and j along the x and y directions, respectively. Each of these sites is characterized by its horizontal size l (identical along the x and y directions and identical for all sites) and the associated aperture $b_{i,j}$, which is the height of the corresponding parallelepipedic box, as well as by connections to its four neighbors with connection areas A_{i,j^-}, A_{i,j^+}, $A_{i^-,j}$, and $A_{i^+,j}$. The connection areas are calculated by multiplying the site length l by the smaller of the two neighboring apertures; for example, $A_{i,j^-} = l\min(b_{i,j}, b_{i,j-1})$. See Figure 2 for a schematic of the lattice representation. The domain has dimensions $L_x \times L_y = n_x l \times n_y l$, where n_x and n_y are the number of sites in the x and y directions, respectively. The total volume V of the fracture void space is $L_x L_y \bar{b}$, where $\bar{b}$ is the arithmetic mean of the aperture distribution.

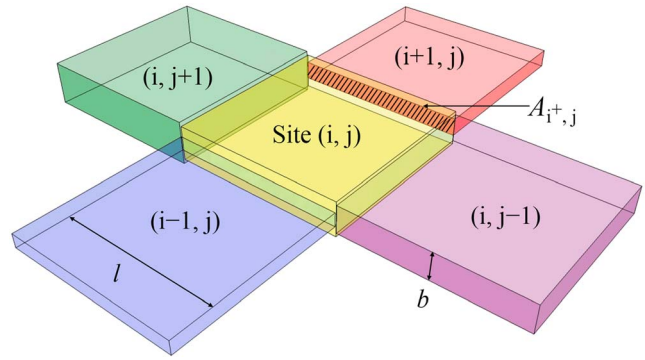

Figure 2. Schematic of the lattice representation of the space between the fracture walls.

2.1.2. Curvatures of Interface and Capillary Pressure Jump

The capillary pressure threshold p^c at a given site (x_{int}, y_{int}) of the interface is calculated locally according to the Young-Laplace equation as

$$p^c(x_{int}, y_{int}) = \gamma \left(\frac{1}{r_1(x_{int}, y_{int})} + \frac{1}{r_2(x_{int}, y_{int})} \right) = \gamma \left(\frac{2\cos\theta}{b(x_{int}, y_{int})} + \frac{1}{r_2(x_{int}, y_{int})} \right), \tag{1}$$

where γ is the interfacial tension, r_1 and r_2 are the two principal radii of curvature at the position considered, b is the local aperture, and θ is the equilibrium contact angle. This capillary pressure threshold is in effect the pressure jump that would exist across the interface if it were locally at equilibrium (i.e., not moving) at this site. It thus corresponds to the threshold value that has to be overcome for the interface to be displaced at the interface site in question. Note that in this model, an interface site is defined as a site that is adjacent to a fully invaded site and contains any nonzero volume of the defending fluid. Following previous works (Glass et al., 1998; Neuweiler et al., 2004; Yang et al., 2012), $1/r_1$ is referred to as out-of-plane (aperture-spanning) curvature and $1/r_2$ as in-plane curvature. See Figure 3 for a schematic of the interfacial curvatures. Note that the in-plane curvature depends on the interface configuration in the direction of the mean fracture plane and needs to be updated whenever the fluid-fluid interface has evolved during the immiscible displacement (the interface evolution resulting from the displacement at each step is described below in section 2.1.4). Hence, the in-plane curvatures contribute nonlocally to the interfacial tension, and the capillary pressure threshold is thus not solely controlled by the local fracture geometry, but also by the history of the displacement. To track the in-plane curvature evolution, we use the algorithm of Yang et al. (2012), which dynamically computes the radius of in-plane curvature along the interface by circle fitting. In the calculation of capillary pressure threshold for each interface site, we set the location of the in-plane curvature at the connection between a fully invaded site and a noninvaded or partially invaded site. Note that for simplicity we only update the local interface location when a site is completely filled.

2.1.3. Solution of Pressure Distribution

We solve the two-dimensional pressure distribution in the fracture via a finite volume scheme (i.e., fluxes are defined on the faces of grid-blocks and pressure is solved at the center of grid-blocks or sites), taking

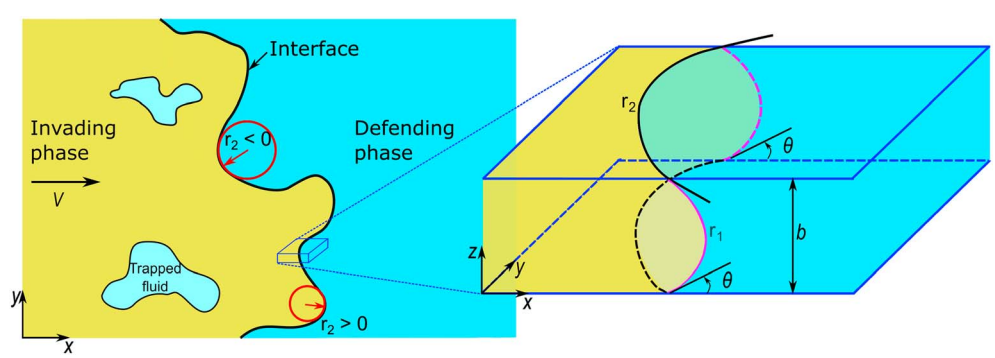

Figure 3. Schematic of the fluid-fluid interface in a fracture, featuring the in-plane and out-of-plane curvatures.

into account the capillary pressure jump at the fluid-fluid interface. The viscosities of the invading and the defending fluids are μ_{inv} and μ_{def}, respectively. The two fluids are assumed immiscible, and plane Poiseuille flow (i.e., a parabolic velocity profiles between the plates) is assumed valid locally within each site box. If no fluid-fluid interface (and hence, no capillary pressure) has to be considered at the connection between two neighboring aperture sites, (i,j) and (i,j^+), the flow rate q across that connection is related to the viscous pressure drop $(p_{i,j} - p_{i,j+1})$ between the two sites and the conductance C of the connection according to

$$q_{i,j^+} = C_{i,j^+} \frac{p_{i,j} - p_{i,j+1}}{l}, \tag{2}$$

where p is the pressure and l is the grid length. If a fluid-fluid interface has to be considered at the connection between the two sites, the calculation of the local flow rate q must take into account a capillary pressure threshold defined by equation (2), as follows:

$$q_{i,j^+} = C_{i,j^+} \frac{\max(0, p_{i,j}^{\text{inv}} - p_{i,j+1}^{\text{def}} - p_{i,j^+}^{\text{c}})}{l} \text{Âă}, \tag{3}$$

where $p_{i,j}^{\text{inv}}$ is the pressure at the invading site (i,j) and $p_{i,j+1}^{\text{def}}$ is the pressure at the defending site $(i,j+1)$. Similarly, equations (2) and (3) can be written for q_{i,j^-}, $q_{i^-,j}$, and $q_{i^+,j}$. The flux equation, equation (3), is *nonlinear* in the sense that the interface does not move if the pressure drop is smaller than the capillary pressure threshold. The capillary pressure threshold p_{i,j^+}^{c} (and similarly, p_{i,j^-}^{c}, $p_{i^-,j}^{\text{c}}$, and $p_{i^+,j}^{\text{c}}$) is calculated based on equation (1) if the connection (i,j^-) is occupied by a fluid-fluid interface. Otherwise, $p_{i,j^+}^{\text{c}} = 0$. The conductance C_{i,j^+} (and similarly, C_{i,j^-}, $C_{i^-,j}$, and $C_{i^+,j}$) is given by

$$C_{i,j^+} = (2A_{i,j^+}) / \left(\frac{\mu_{i,j}}{k_{i,j}} + \frac{\mu_{i,j+1}}{k_{i,j+1}} \right), \tag{4}$$

where $k_{i,j}$ and $k_{i,j+1}$ are the permeabilities ($k = b^2/12$) and $\mu_{i,j}$ and $\mu_{i,j+1}$ are the averaged viscosity weighted by the volume fraction of each phase at site (i,j) and $(i,j+1)$, respectively.

Based on the incompressible fluid assumption, we can now write the general volume conservation equation for each aperture site (i,j):

$$q_{i^-,j} + q_{i^+,j} + q_{i,j^-} + q_{i,j^+} = Q_{i,j}, \tag{5}$$

where $Q_{i,j}$ is a source term for site (i,j). As the fluids are assumed incompressible, source flux terms appear only at the boundaries of the domain. Writing equation (5) for all sites and putting in the flux equations 2 and (3) gives a system of equations which need to be solved for the pressure distribution, given a certain set of conditions at the boundaries of the domain. A complication arises due to the capillary pressure jump condition at fluid-fluid interfaces as one substitutes the nonlinear flux equation, equation (3) into equation (5). The *max* function prevents a direct solution of the pressure from equation (5). Hence, we use an iterative approach to obtain the pressure solution of equation (5). Indeed, at each time step we use the pressure distribution from the last time step to evaluate the *max* function at all grids along the fluid-fluid interface, that is, to determine whether the interfacial flux at each connection is zero or positive. With this information we solve the conservation equation (5) for pressure and update the signs and values of the interfacial fluxes. This process is repeated n_{iter} (number of iterations) times until a satisfactory pressure solution is obtained. One can check the pressure field convergence by using the criterion $||\mathbf{p}_{\text{new}} - \mathbf{p}_{\text{old}}/||\mathbf{p}_{\text{old}} < \varepsilon$, where ε is a tolerance and $\mathbf{p}_{\text{old}}$ and $\mathbf{p}_{\text{new}}$ are the pressure solution before and after an iteration, respectively. We have tested the effect of n_{iter} on the displacement patterns and we find that the difference between the simulated patterns obtained with a fixed $n_{\text{iter}} = 4$ and with a tolerance $\varepsilon = 10^{-4}$ are satisfactorily small (see supporting information Figures S1–S2). In this study, we use a fixed $n_{\text{iter}} = 4$ for simulations of the experimental configurations and a parametric investigation where the viscosity ratio, the capillary number, and the contact angle are varied. As a reference, the pore-network simulations of Lenormand et al. (1988) used four iterations to obtain the pressure solution at each time step.

2.1.4. Flow Rules

2.1.4.1. Front advancement:

The iterative solution of the volume conservation equation gives a pressure field, from which we explicitly compute the fluxes along the fluid-fluid interface using equation (3). At the start of each time step, we know the fraction of the volume occupied by the invading fluid $f_{i,j}$ at each site (i,j). Knowing the invading status

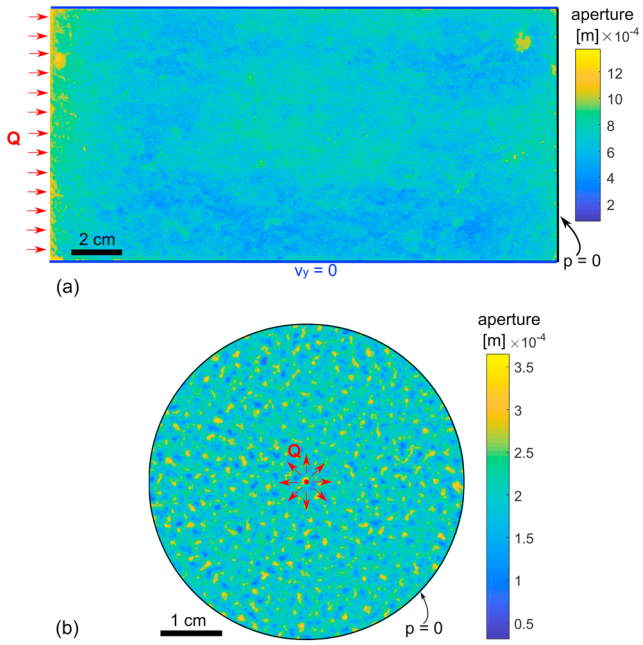

Figure 4. (a) Aperture field (of standard deviation 0.12 mm) and boundary conditions used to simulate the parallel flow experimental configuration of Y.-F. Chen et al. (2017) and confront its results to their experimental measurements; (b) aperture field and boundary conditions used for the simulations of a radial injection scenario.

and fluxes at all interfacial sites, we can evaluate the time required to fill each interfacial site box. The time step Δt is then calculated as the smallest time required to completely fill one interfacial site box. The invading fluid flows into all interface sites ($0 < f < 1$) that have at least one connection with a positive flow rate, until one of the interface sites reaches $f = 1$. The change in volume fraction $\Delta f_{i,j}$ for each interface site (i,j) due to fluid invasion at each time step is calculated as

$$\Delta f_{i,j} = \frac{\Sigma q_{i,j}^{\text{interf}} \Delta t}{V_{i,j}}, \tag{6}$$

where $V_{i,j}$ is the volume of parallelepipedic box associated to the local site and $\Sigma q_{i,j}^{\text{interf}}$ represents the sum of the interfacial fluxes from the invading neighbors to the local defending site (i,j). During drainage, when the injection rate or the injection pressure is low, $\Sigma q_{i,j}^{\text{interf}}$ can be zero at many sites if there is a large capillary resistance. When f reaches 1 at one site, the interface location is updated accordingly. After each time step, we update the fluid-fluid interface and recalculate the capillary pressure threshold across the interface according to equation (1). Note that for simplicity, we do not consider the influence of partially invaded sites on the capillary pressure thresholds, since the exact configuration of fluid distribution in a partially invaded site is unknown and could in any case only be approximated. It is further assumed that once a site is fully invaded, it remains fully invaded at all subsequent time steps. In other words, counterinvasion is not allowed, which is a simplifying assumption to ease the implementation of the algorithm in terms of trapping and interface tracking.

2.1.4.2. Trapping rules:

Trapping of the defending fluid, at or above the length scale of a site, is taken into account (Yang et al., 2016); this means that the defending fluid-occupied sites that are surrounded by the invading fluid become uninvadable, stationary blobs. An efficient bidirectional search algorithm is implemented to check the trapping condition after each time step. Note that in this model, we do not consider remobilization of the trapped defending phase.

2.2. Brief Description of the Experiment

In section 3.2 below we confront recently published experimental data (Y.-F. Chen et al., 2017) to numerical simulations of the experimental geometry. Here, we briefly describe these experiments. Y.-F. Chen et al. (2017) carried out visualization experiments of immiscible displacement using transparent resin replicas of a rock fracture obtained from a Brazilian test. The transparent fracture had rough walls and a mean aperture of 0.66 mm measured by the total fluid volume method. The reported standard deviation of the aperture field was 0.12 mm. This standard deviation was considered an underestimation due to the inaccurate aperture calculations from the absorbed light by the dye. It is not possible to obtain the exact standard deviation, but it is deemed reasonable that the real standard deviation could be at least 50% higher. Therefore, in the simulations here, we also consider a second fracture geometry with a higher standard deviation of 0.18 mm. The aperture field with the higher standard deviation is obtained by scaling the difference between the originally reported aperture field and its mean by a factor of $0.18/0.12 = 1.5$. Since the fracture replicas were hydrophobic, the invading water was the nonwetting phase and the defending fluid of silicone oil is the wetting phase, so all runs of the experiment were under drainage condition. Silicone oils of different viscosities and different water injection rates were used, resulting in an experimental parameter space encompassing various viscosity ratios and capillary numbers. The invading water entered the fracture from its left edge through an inlet reservoir and displaced the defending silicone oil toward its right edge subjected to atmospheric pressure conditions. The top and bottom edges of the domain were no flow boundaries. The viscosity of water is lower than that of silicon oil, so that the displacement is expected to generate fingering patterns both in the capillary- and the viscous-dominated flow regimes. The aperture field (of standard deviation of 0.12 mm) and the boundary conditions are depicted in Figure 4a. The simulation parameters are listed in Table 1. In the simulations, a flux boundary is applied at one side of the domain,

Table 1
Parameters Used to Simulate the Experimental Parallel Flow Configuration

Parameters	Value
Mean aperture $\langle b \rangle$	0.66 mm
Aperture field standard deviation σ_b	0.12, 0.18 mm
Fracture size L_x, L_y	200, 100 mm
Viscosity of silicone oil μ_{def}	500, 100 mPa·s
Viscosity of water μ_{inv}	1.0 mPa·s
Interfacial tension γ	35.0 mN/m
Equilibrium contact angle θ	46° (drainage)
Injection rate Q	0.01, 0.1, 0.3, 1, 10 ml/min
Capillary number $\log_{10}\text{Ca}$	−7.07, −6.07, −5.59, −5.07, −4.07
Grid size of simulations l	0.4 mm

a constant pressure condition at the opposite side and no flow boundaries at the remaining sides. A column of cells with large volume, representing the inlet reservoir, is placed at the constant flux boundary side. Due to the small resistance of these cells, the fluid pressure does not vary much between these cells. The fluxes into the individual adjacent cells in the fracture are determined by the capillary pressure thresholds and the pressure gradients from the inlet cells to the adjacent cells.

2.3. Simulations of a Radial Injection Scenario

In addition to the validation of the numerical model by comparison to parallel flow experiments, we have simulated immiscible displacement in a scenario where the injection happens at the center of the fracture domain. In these radial injection simulations, spatially correlated random aperture fields have been generated according to the model proposed by Brown (1995). The topography of the fracture wall surfaces has a power spectrum of the form

$$G(\xi_x, \xi_y) \propto (\xi_x^2 + \xi_y^2)^{-(H+\frac{1}{2})}, \tag{7}$$

where ξ_x and ξ_y are the wave numbers in the x and y dimensions, H is the Hurst exponent, which is characteristic of the fracture walls' self-affinity ($H = 0.8$ here). An inverse fast Fourier transform method is used to generate the topography of these walls. We define a cutoff wave number (spatial frequency) ξ_c below which two rough-wall surfaces have identical Fourier spectra. This way, the two surfaces are matched at small wave numbers (i.e., long wave lengths), resulting in apertures (gaps between two surfaces) that are spatially correlated at length smaller than a correlation length $l_c \propto 1/\xi_c$, and do not vary significantly above that length. We set the mean and the standard deviation of apertures to be $\langle b \rangle = 200\ \mu$m and $\sigma_b = 40\ \mu$m, respectively. We first generate an aperture field of 256×256 and then consider only the region inside a circle of radius $D/2$. The aperture field and the associated boundary conditions for flow are depicted in Figure 4b. Compared

Table 2
Parameters Used for Simulations of the Radial Scenario

Parameters	Value
Fracture aperture b, (mean ± std)	(0.2 ± 0.04) mm
Fracture size D	51.2 mm
Cutoff wave number ξ_c	16
Hurst exponent H	0.8
Viscosity ratio $M = \mu_{\text{inv}}/\mu_{\text{def}}$	0.005, 0.05, 0.5, 5
Interfacial tension γ	35.0 mN/m
Equilibrium contact angle θ	0°, 60° (drainage)
Injection rate Q	0.01, 0.1, 1, 10, 100 ml/min
Capillary number (radial) $\log_{10}\text{Ca}^*$	−6.83, −5.83, −4.83, −3.83, −2.83
Grid size l	0.2 mm

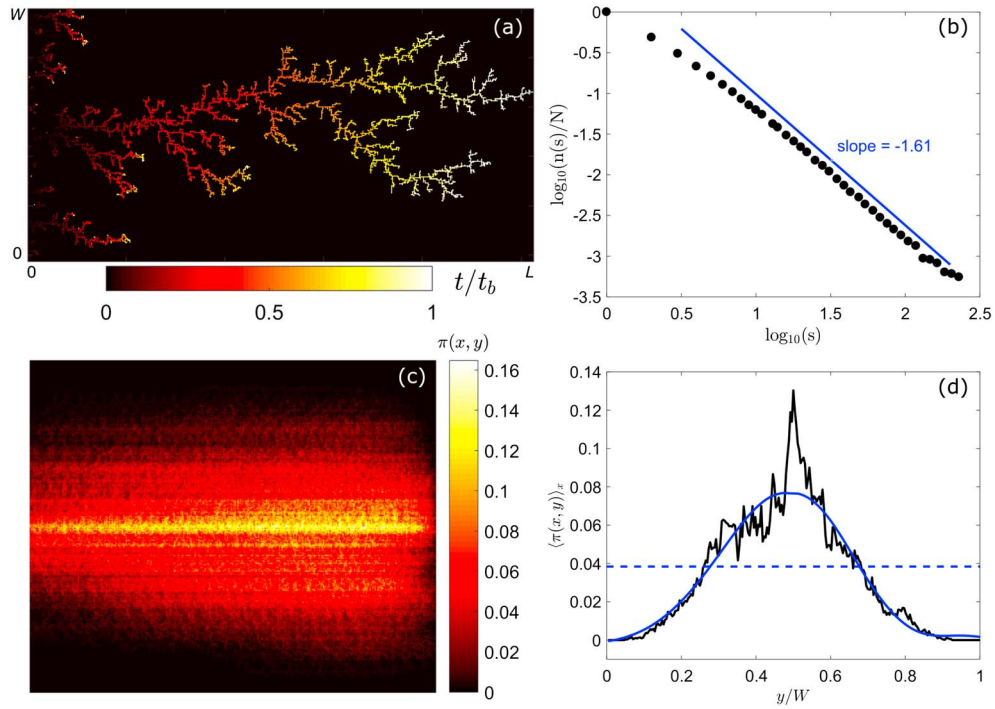

Figure 5. (a) Invasion pattern obtained when simulating high M drainage in a geometry analogous to that of a 2-D random porous medium (of width W and length L, 256*512 pixel units) and without accounting for the in-plane curvature contribution in the capillary pressure. (b) Average box-counting plot obtained from eight independent simulations similar to that of (a). (c) Average map of the occupancy probability in the reference frame of the most advanced fingertip, obtained from these eight experiments. (d) Transverse profile of the occupancy probability map (c), obtained by averaging it along the longitudinal direction; the width at half-maximum of the profile filtered for high wavelength noise is 0.39.

with the aperture field measured in the experiment, the synthetic aperture field here has a well-defined spatial correlation and a smaller mean aperture, while the coefficient of variation $\sigma_b/\langle b\rangle$ is almost the same. The parameters used for the simulations in this scenario are listed in Table 2.

3. Results

3.1. Simulation of Viscous Fingering in a Random Noncorrelated Aperture Field

In order to validate the model and show that it accounts for viscous effects properly, we first consider high capillary number drainage ($\log_{10}\mathrm{Ca} = -3.7$) in a random, Gaussian, aperture field that has no spatial correlations, and in which 25% of the grid sites have been assigned a zero aperture. We thus consider fracture configurations that are akin to a two-dimensional porous medium. We furthermore deliberately turn off the accounting of the capillary pressure contribution from the in-plane curvature, and consider a large viscosity ratio $M = 1,000$. We thus expect to address flow phenomenologies that are perfectly analogous to viscous fingering at large M in random two-dimensional porous media. The properties of invasion patterns obtained in such configuration, such as the one shown in Figure 5a, are well known, in particular we expect a fractal dimension close to 1.62 (as first measured by Måløy et al., 1985, with a 0.04 uncertainty), and the dynamics of the growth process has been studied in detail by Løvoll et al. (2004) and Toussaint et al. (2005). From eight different porous media of identical statistical properties, we measure the average box-counting curve shown in Figure 5b, which yields a fractal dimension of 1.61 ± 0.03, in excellent agreement with the value from the literature. From the eight independent numerical runs we also measure the average map of occupancy probabilities $\pi(x,y)$ for the displacing fluid in the reference frame attached to the tip of its most advanced finger (see Toussaint et al., 2005). A cut of the $\pi(x,y)$ topography (see Figure 5d) at its half-maximum value provides the shape of the *envelope* of the flow pattern, which looks similar to a Saffman-Taylor finger but with a width 0.39 W, where W is the width of the medium, as evidenced from the mean transverse cut of the topography presented in Figure 5d. This value differs from the 0.5 W value expected for the Saffman-Taylor

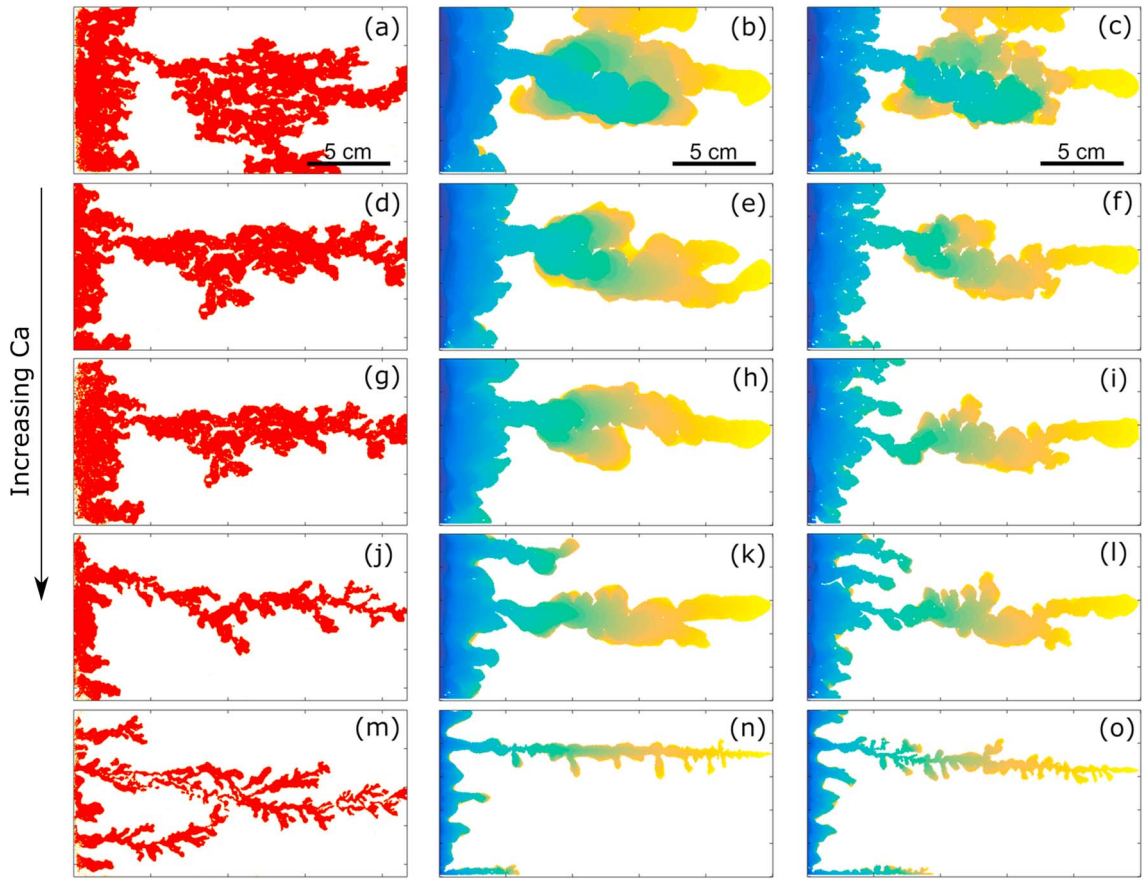

Figure 6. Immiscible displacement patterns at breakthrough for the case $M = 1/500$. (a, d, g, j, and m) experimentally patterns observed for flow rate of 0.01, 0.1, 0.3, 1, 10 ml/min (corresponding to capillary numbers $\log_{10}\mathrm{Ca} = -7.07, -6.07, -5.59, -5.07, -4.07$) from top to bottom. (b, e, h, k, and n) simulated patterns obtained with the aperture field of standard deviation 0.12 mm. (c, f, i, l, and o) simulated patterns obtained with the aperture field of standard deviation 0.18 mm. The flow rates are identical to those used in the experiments. Colors from blue to yellow represent invading times from start to breakthrough.

configuration (i.e., in a parallel plate geometry; Saffman & Taylor, 1958). The width of the envelope has been shown to be a subtle measure of the invasion dynamics, hence we demonstrate here that our numerical model describes the action of viscous forces properly.

3.2. Comparison of Displacement Patterns Between Experiments and Simulations

Two sets of simulations are reported here, using two aperture fields of standard deviations 0.12 and 0.18 mm, respectively. In the following, we refer to these two sets as simulation set 1 and simulation set 2. Figure 6 presents the comparison between experimental observations and simulated results in terms of the displacement patterns at breakthrough for the case of a viscosity ratio $M = 1/500$. The capillary number spans three orders of magnitude in these experiments, ranging from $\log_{10}\mathrm{Ca} = -7.07$ to $\log_{10}\mathrm{Ca} = -4.07$. It is shown in Figure 6 that in general the numerical model is able to reproduce the essential features of experimentally observed patterns using both aperture fields, of different standard deviations. In particular, both the experiments and the simulations show that the invading finger of the nonwetting phase becomes thinner as the capillary number (or flow rate) increases. When the capillary number is small ($\log_{10}\mathrm{Ca} < -5.59$, Figures 6a–6c), the invasion is dominated by capillary forces, and the invading nonwetting fluid tends to occupy the large-aperture regions along the flow pathway, which is characteristic of capillary fingering. As the capillary number gradually increases, viscous forces become more and more important compared to capillary forces. When $\log_{10}\mathrm{Ca} \geq -5.07$ (Figures 6j–6l), the invasion pattern can be characterized as being in a crossover regime according to Y.-F. Chen et al. (2017), thus approaching a viscous fingering regime. Comparison between the two sets of simulations reveals that increasing the standard deviation of the aperture field leads to displacement patterns that better match the experiment in terms of the front roughness and fluid trapping. Note that it is not possible to match all the fine details of the patterns between the experiments and

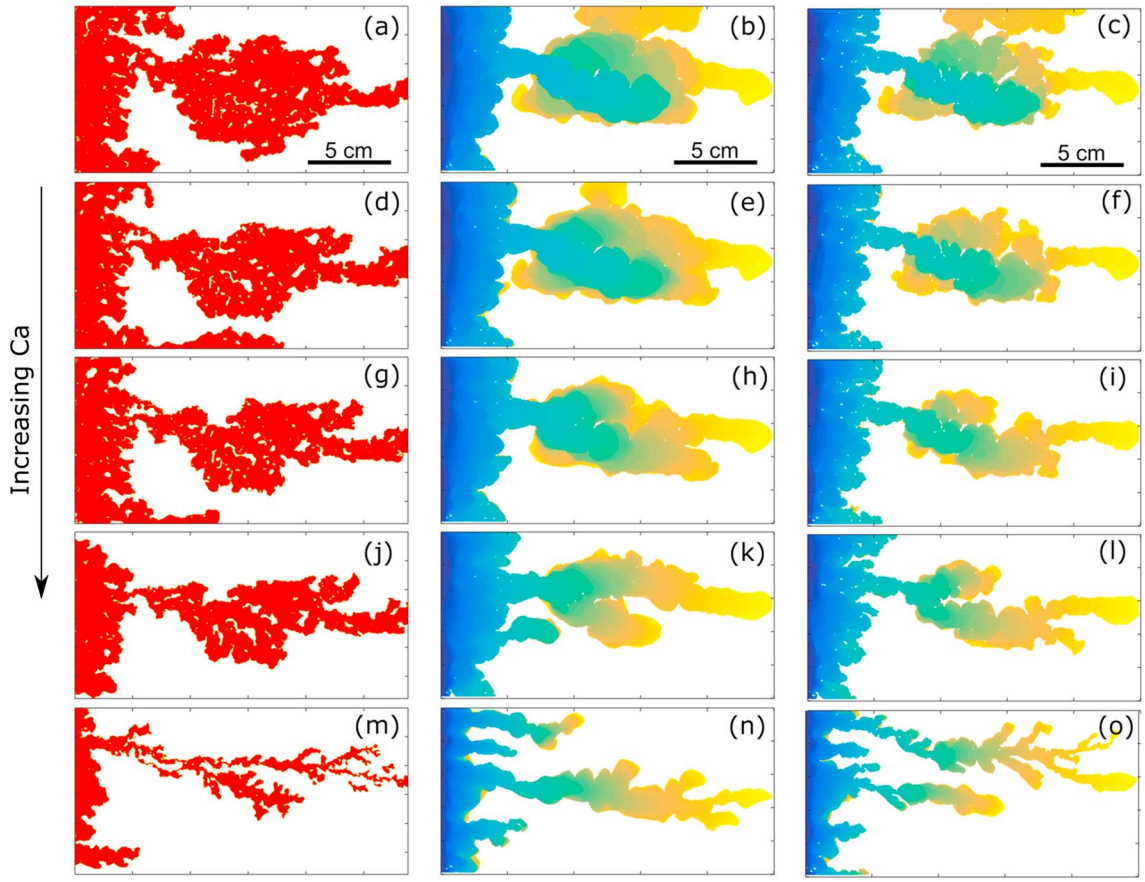

Figure 7. Immiscible displacement patterns at breakthrough for the case $M = 1/100$. (a, d, g, j, and m) experimentally patterns observed for flow rate of 0.01, 0.1, 0.3, 1, 10 ml/min (corresponding to capillary numbers $\log_{10}\mathrm{Ca} = -7.07, -6.07, -5.59, -5.07, -4.07$) from top to bottom. (b, e, h, k, and n) simulated patterns obtained with the aperture field of standard deviation 0.12 mm. (c, f, i, l, and o) simulated patterns obtained with the aperture field of standard deviation 0.18 mm. The flow rates are identical to those used in the experiments. Colors from blue to yellow represent invading times from start to breakthrough.

the simulations, because the aperture field measurement technique induces measurements errors (Detwiler et al., 1999; in addition to instrumental uncertainties on the measurements) and the invasion pathways are sensitive to perturbations in the aperture field. This is no surprise as it was already shown, in similar unstable flow configurations in two-dimensional porous media, that even uncertainties on an experimental geometry are sufficient to prevent full deterministic prediction of the displacement pattern by CFDs (Ferrari et al., 2015). The simplifying assumptions relevant to the comparison between the simulated and experimentally observed patterns will be discussed further in section 4.

For the case of $M = 1/100$, we have also compared the breakthrough displacement patterns between the experiments and the simulations using the two aperture fields of different standard deviations (Figure 7). It can be seen that again the simulated results show an overall good match with the experimental patterns. The invasion patterns shift from capillary fingering regime at low capillary numbers ($\log_{10}\mathrm{Ca} < -5.07$) to a transitional regime at the much higher capillary number ($\log_{10}\mathrm{Ca} = -4.07$). The capillary-dominated fingering regime extends to a higher capillary number than in the previous case, which can be explained by the smaller viscous effects at identical flow rate, resulting from the weaker viscosity contrast. It can also be seen that the set of simulations using the aperture field of higher standard deviation results in a displacement pattern that is more similar to the experimental pattern. In the following, we perform quantitative comparison between the simulations and the experiment in terms of displacement efficiencies, invading tip advancement, and fractal dimensions.

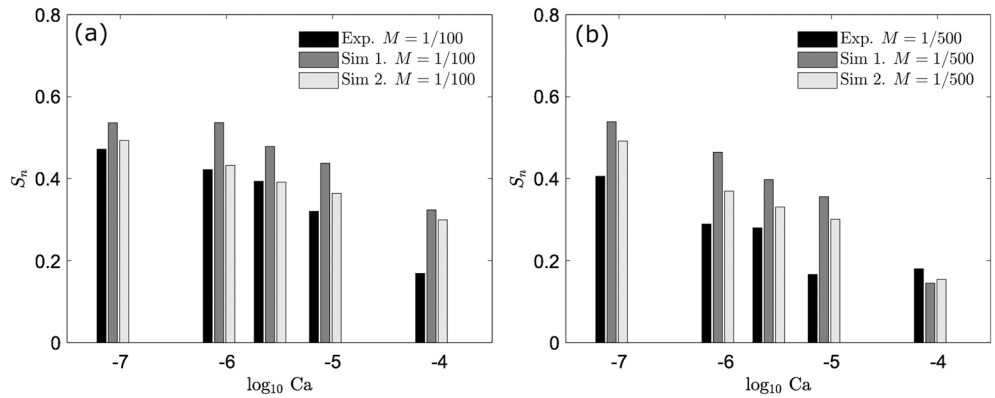

Figure 8. Comparison of areal saturation at breakthrough for cases of (a) viscosity ratio $M = 1/100$ and (b) $M = 1/500$. Two sets of simulations are shown with "Sim 1" (respectively, "Sim 2") denoting those using the aperture field of standard deviation 0.12 mm (respectively, 0.18 mm).

3.3. Displacement Efficiency

We now compare the displacement efficiency E_d between the simulations and the experiments; E_d is defined as the ratio of the area occupied by the nonwetting phase at breakthrough to the total fracture area. In other words, the displacement efficiency is equal to the areal saturation of the nonwetting phase (S_n) at breakthrough time. Figure 8 shows that the evolution of the areal saturation with varying capillary number predicted by the numerical simulations is generally consistent with the measurements for both cases of viscosity ratio. The simulations with the aperture field of higher standard deviation give S_n values that match the experiment more closely. For the case of $M = 1/100$ (Figure 8a), the relative error in areal saturation at breakthrough for simulation set 2 (with higher aperture standard deviation) mostly ranges between 0.3% and 12.5%, with the exception of $\log_{10}\text{Ca} = -4.07$ where the simulation strongly overestimates the areal saturation due to the thicker fingers simulated. For the case of $M = 1/500$ (Figure 8a), the saturation comparison is not as good as in the previous case; the relative error for simulation set 2 ranges between 15% and 20% with the exception at $\log_{10}\text{Ca} = -5.07$ where the simulated fingers are thicker than those in the experiment. Note that the saturation could also be computed by the volumetric way, that is volume of nonwetting phase—computed as $l^2\sum_{(i,j)\text{in nw phase}} a_{i,j}$—divided by total volume of the fracture at breakthrough. This saturation is slightly higher (by 0.02–0.04) than the displacement efficiency (areal saturation) since the nonwetting fluid prefers to occupy the large-aperture regions.

3.4. Invading Tip Advancement

The effect of the competition between capillary and viscous forces can also be studied by considering the characteristics of the invading tip advancement along the x direction. Here we do so by plotting the normalized invading phase saturation ($S_{\text{inv}}/\max(S_{\text{inv}})$) as a function of the normalized tip location $x^*_{\text{tip}} = x_{\text{tip}}/L_x$. In Figure 9 such plots are shown both for the experiments (Figures 9a and 9b) and for the numerical results (Figures 9c–9f), and for two viscosity ratios (Figures 9a, 9c, and 9e: $M = 1/100$, Figures 9b, 9d, and 9f: $M = 1/500$). The behavior as seen in the simulations is generally consistent with that in the experiments. For strongly capillary-dominated flows (e.g., $\log_{10}\text{Ca} = -7.07$), the S_{inv}–x^*_{tip} curve is characterized by frequent vertical jumps of various sizes controlled by the distribution of apertures in the fracture. In the simulations with $\log_{10}\text{Ca} = -7.07$, the average size of largest five jumps in $S_{\text{inv}}/\max(S_{\text{inv}})$ is about 0.067 (for $M = 1/100$) and 0.055 (for $M = 1/500$) for Simulation set 1 and 0.065 (for $M = 1/100$) and 0.059 (for $M = 1/500$) for Simulation set 2. These results are in reasonably good agreement with the experiment (0.058 for $M = 1/100$ and 0.069 for $M = 1/500$). As the flow rate (capillary number) gradually increases, the jumps decrease in size and eventually disappear for $\log_{10}\text{Ca} = -4.07$. Figure 9 also shows that the stronger the viscosity contrast, the smoother the S_{inv}–x^*_{tip} curve for a given capillary number. The staircase-like structure of the S_{inv}–x^*_{tip} curve in the capillary-dominated invasion can be explained by the flow of the nonwetting invading phase in all directions, especially in the transverse and backward directions, after the front overcomes a relatively large capillary resistance of a narrow aperture site and sees connected large-aperture zones. Viscous forces tend to smoothen the staircase-like structure, as they promote invasion toward the outlet and suppress the front advancement in the transverse and backward directions to minimize viscous pressure drops from the front to the outlet through the more viscous defending phase.

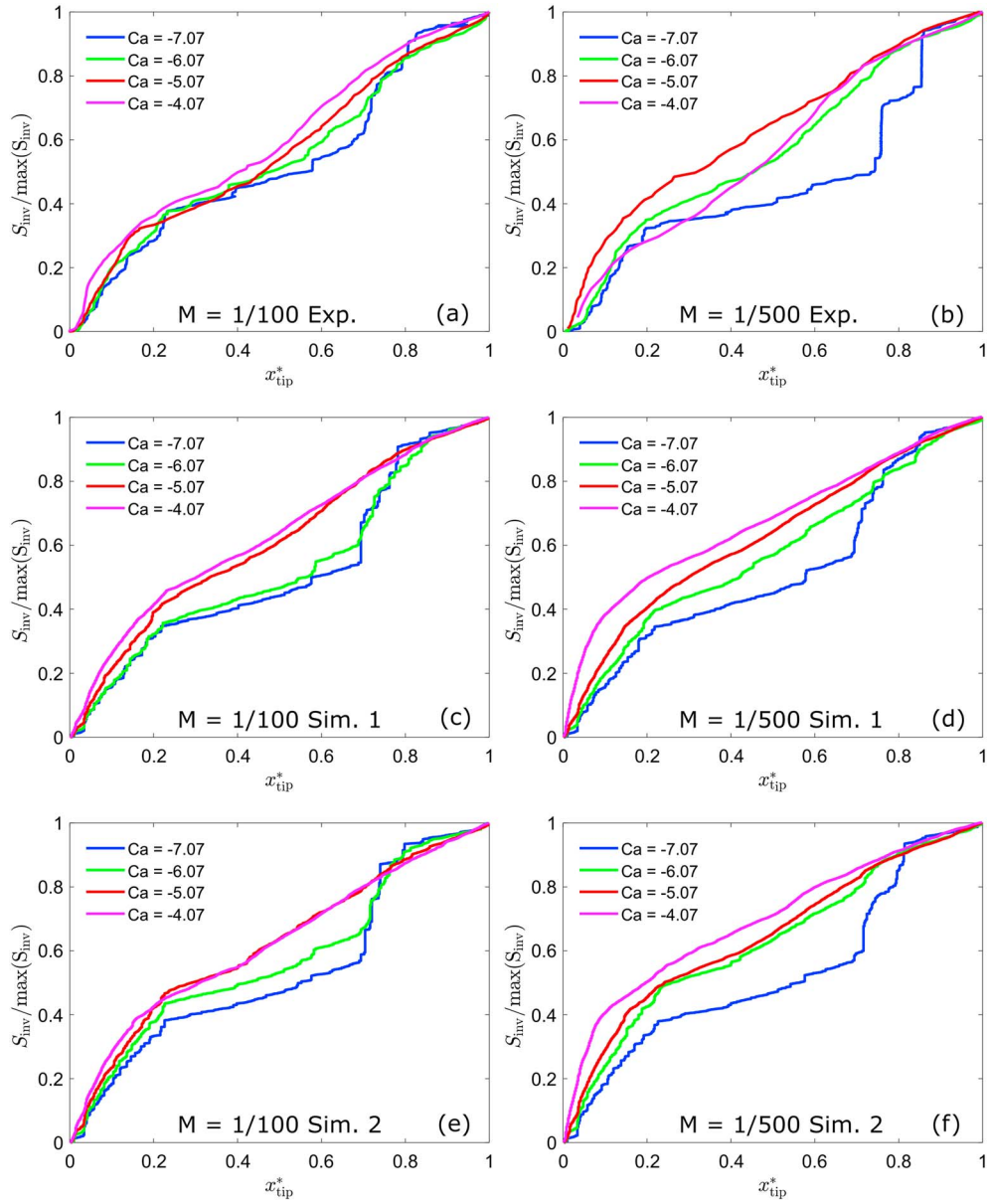

Figure 9. Evolution of the normalized invading phase saturation ($S_{inv}/\max(S_{inv})$) as a function of the normalized tip location (x^*_{tip}) in the experiments (a and b) and numerical simulations (c, d, e, and f) and for two viscosity ratios: $M = 1/100$ and $M = 1/500$. Two sets of simulations are shown with "Sim 1" (respectively, "Sim 2") denoting those using the aperture field of standard deviation 0.12 mm (respectively, 0.18 mm).

3.5. Box-Counting Fractal Dimension

The invading patterns resulted from the competition between capillary and viscous forces exhibit different space-filling characteristics which can be measured by fractal dimension. Figure 10 presents the fractal dimension of the invading fluid calculated using the box-counting method. It can be seen that the simulations well capture the general trend that the fractal dimension decreases with increasing capillary number. For $M = 1/100$, the fractal dimension for both the experiment and simulation drops from $D_f \approx 1.84$ at $\log_{10}\text{Ca} = -7.07$ to $D_f \approx 1.63$ at $\log_{10}\text{Ca} = -4.07$. These fractal dimensions fall in the respective ranges of values for the classical capillary fingering and viscous fingering regimes in 2-D porous media (see e.g., King, 1987; Måløy et al., 1985; Wilkinson & Willemsen, 1983). For $M = 1/500$, the fractal dimensions show good agreement between the experiment and the simulations for $\log_{10}\text{Ca} \leq -5.59$. For the two high capillary number cases, the match in fractal dimensions is not as good.

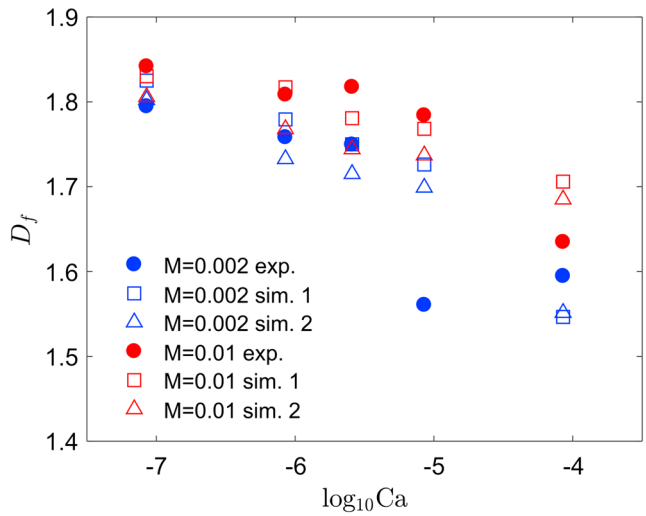

Figure 10. Comparison of box-counting fractal dimension between experiments and simulations. Two sets of simulations are shown with "Sim 1" (respectively, "Sim 2") denoting those using the aperture field of standard deviation 0.12 mm (respectively, 0.18 mm).

3.6. Fluid Pressure

Our numerical simulations provide information on fluid pressure distributions which could not be measured in the experiment. Here, we only show the simulated pressure distribution using the aperture field with standard deviation of 0.18 mm, since the results for the low aperture standard deviation are similar. Figure 11 presents the pressure distributions where a few observations can be made: (i) as expected, the invading pressure and the pressure gradient are higher for flows with larger capillary numbers (note the different colorbar scales); (ii) when the capillary number is very small (Figure 11a), the pressure is almost uniform (pressure gradient Δp is almost zero) within each phase, and the pressure difference between the two phases is mostly equal to the capillary pressure at the interface; as the capillary number increases (Figures 11c, 11e, 11g, and 11i), the pressure gradient within each viscous phase also increases; (iii) since the viscosity is much larger in the defending phase than in the invading phase, the pressure drop is mainly visible in the defending phase.

To better understand the competition between capillary and viscous forces, it is useful to compare the capillary pressure with the viscous pressure drop over a certain length scale (e.g., the front width extension, taken as the distance, in the x direction, between the advancing tip and the trailing front). The capillary pressure calculated according to equation (1) using the mean aperture as a characteristic length is on the order of 10^2 Pa. The capillary pressure variation over one standard deviation of the local apertures is about 35 Pa. The viscous pressure drop through the more viscous defending phase is proportional to the mean flow velocity; for example, when $\log_{10}\text{Ca} = -5.07$ ($V = 1.26 \times 10^{-4}$), the viscous pressure drop is estimated to be $w_f \mu_{def} V/\bar{k} = 35$ Pa for a front width $w_f = L_x/2$ and choosing the viscosity to $\mu_{def} = 100$ mPa·s. These calculations indicate that for $\log_{10}\text{Ca} \leq -5.59$ and $M = 1/100$, the flow is dominated by the capillary forces. For $\log_{10}\text{Ca} = -5.07$, the viscous pressure drop is only comparable to the capillary pressure variation at a length scale larger than $L_x/2$, meaning that capillary forces have a stronger influence on the invasion dynamics than viscous forces. Starting with the case of $\log_{10}\text{Ca} = -4.07$, the viscous forces will start to play a more and more dominant role in shaping the invasion pattern.

The simulated pressure distributions for the case $M = 1/500$ are presented in Figure 12. Similar trends can be noted as in the case of $M = 1/100$ (Figure 11), and are explained similarly (see above). However, with the increased defending phase viscosity ($\mu_{def} = 500$ mPa·s), the viscous effect starts competing with the capillary effect at a smaller capillary number (here at $\log_{10}\text{Ca} = -5.07$). The displacement patterns for $\log_{10}\text{Ca} = -5.07$ and -4.07 are in the transitional regime between capillary fingering and viscous fingering.

It is notable in Figures 11 and 12 that when the invading fluid has a much smaller viscosity than the defending phase, the pressure gradient in the invading fluid is negligible, even at high capillary numbers. Thus, in

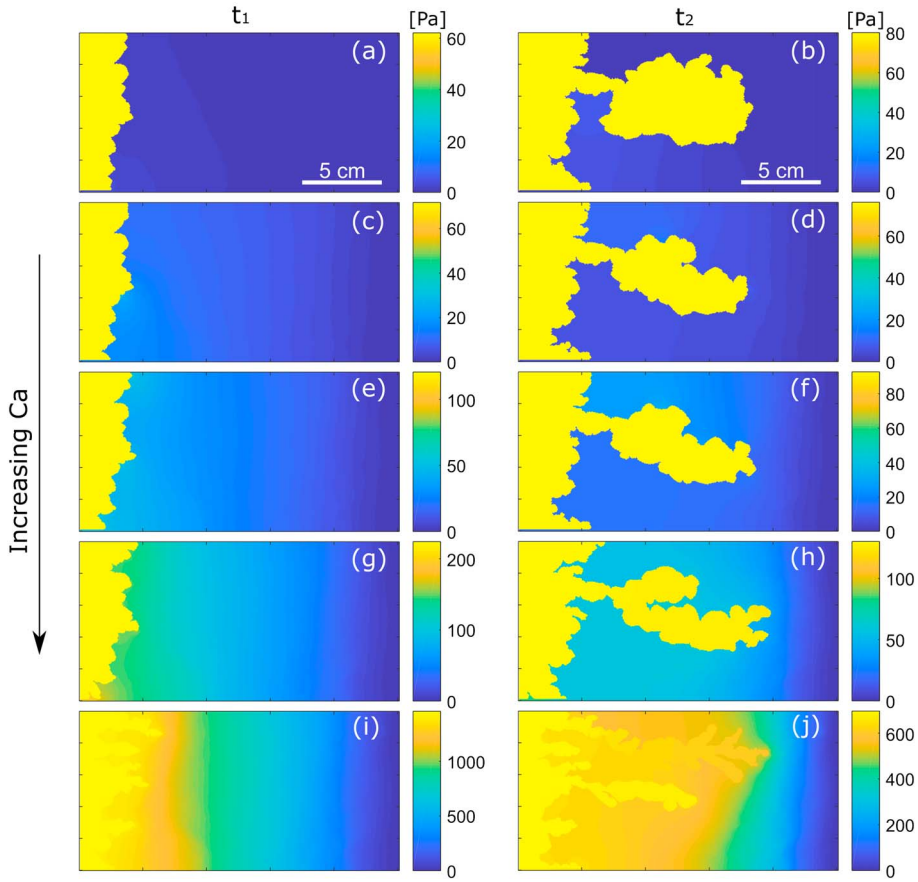

Figure 11. Simulated pressure distributions at two different stages of the displacement process for $M = 1/100$, and for different capillary numbers ($\log_{10}\mathrm{Ca} = -7.07, -6.07, -5.59, -5.07, -4.07$ from top to bottom). The aperture field standard deviation is 0.18 mm. (a, c, e, g, and i) Pressure at an early stage of the invasion process, when fingers are starting to develop; (b, d, f, h, and j) pressure at a later stage, when the prominent finger has developed and extended to $x^*_{\mathrm{tip}} > 0.5$.

this case it is possible to simplify the solution of pressure distribution by assuming that the pressure is the same as the inlet pressure through the invading phase of a high viscosity contrast.

It is also interesting to see how fluid pressure evolves during the whole invasion process. For this, we record inlet pressure p_{in} throughout the simulations (p_{in} is calculated as the average of pressure of all inlet grids). The inlet pressure also equals to the pressure difference between the inlet and outlet, considering that the outlet pressure boundary is zero. Expectedly, the inlet pressure is higher for larger capillary numbers. For the case $M = 1/100$ (Figure 13a), when $\log_{10}\mathrm{Ca} = -4.07$ the inlet pressure decreases significantly as the invading phase saturation increases until breakthrough. This is because the pressure gradient in the more viscous defending phase decreases as the distance from the invading tip to the outlet is gradually shortened due to the front advancement. As the capillary number decreases, capillary forces become more and more important, leading to considerable relative fluctuations in the inlet pressure. In our model runs with constant inflow rate, the inlet pressure oscillates as it must adjust to satisfy the capillary pressure jump conditions along the fluid-fluid interface while the pressure distribution is solved in both phases. Qualitatively, one can also distinguish the viscous-dominated displacement ($\log_{10}\mathrm{Ca} = -4.07$) from capillary-dominated flow ($\log_{10}\mathrm{Ca} < -5.07$) by judging the fluctuation patterns in the inlet-outlet pressure difference and whether the inlet pressure decreases substantially with flow.

For high capillary number flow ($\log_{10}\mathrm{Ca} = -4.07$), when $M = 1/500$ (Figure 13b), the inlet pressure is significantly higher (by a factor of 5) than that obtained in the case $M = 1/100$, because of the increased defending phase viscosity, from 100 to 500 mPa·s. A comparison of Figures 13a and 13b also shows that viscous-dominated flow starts to occur for a lower capillary number when the viscosity contrast is stronger,

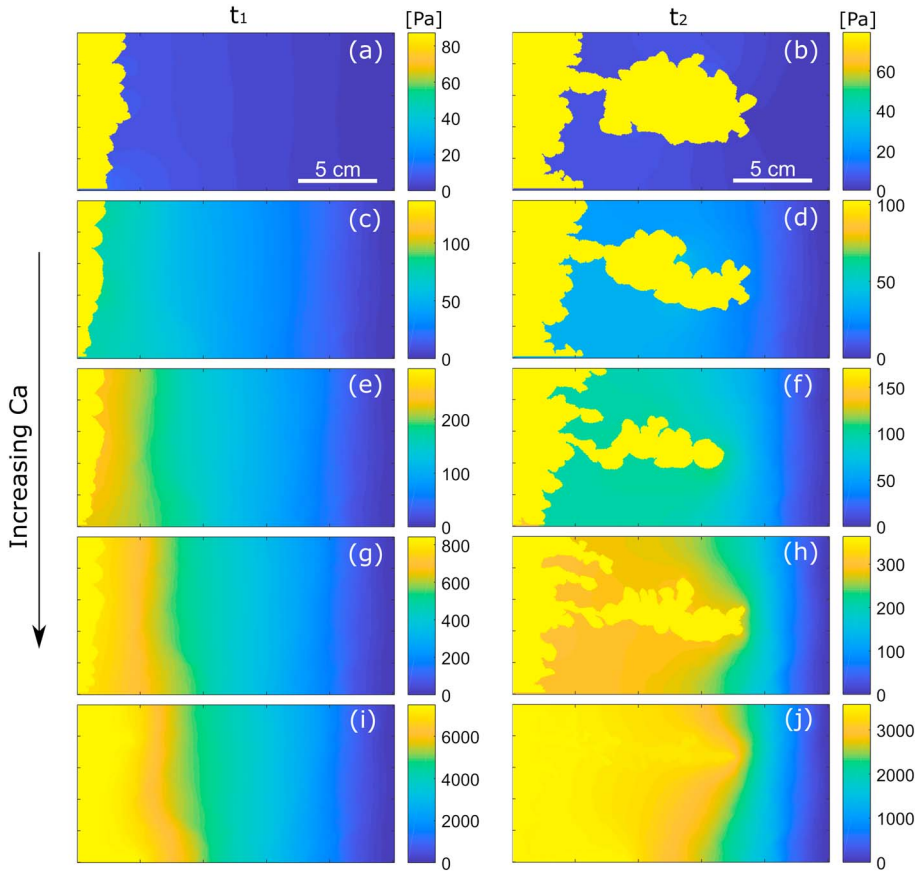

Figure 12. Simulated pressure distributions at two different stages of the displacement process for $M = 1/500$, and for different capillary numbers ($\log_{10}\mathrm{Ca} = -7.07, -6.07, -5.59, -5.07, -4.07$ from top to bottom). The aperture field standard deviation is 0.18 mm. (a, c, e, g, and i) pressure at an earlier stage of the invasion process, when fingers are just starting to develop; (b, d, f, h, and j): pressure at a later stage, when the prominent finger has developed and extended to $x^*_{\mathrm{tip}} > 0.5$.

which is consistent with the observations of displacement patterns and with the theoretic phase diagram of drainage in two-dimensional porous media (Lenormand et al., 1988).

3.7. Pattern Formation of Immiscible Displacement in Radial Scenario

Most of the experiments and simulations of two-phase flow in rough fractures in the literature have employed a rectangular shape of the fracture domain, and usually, the boundaries have been set by injection

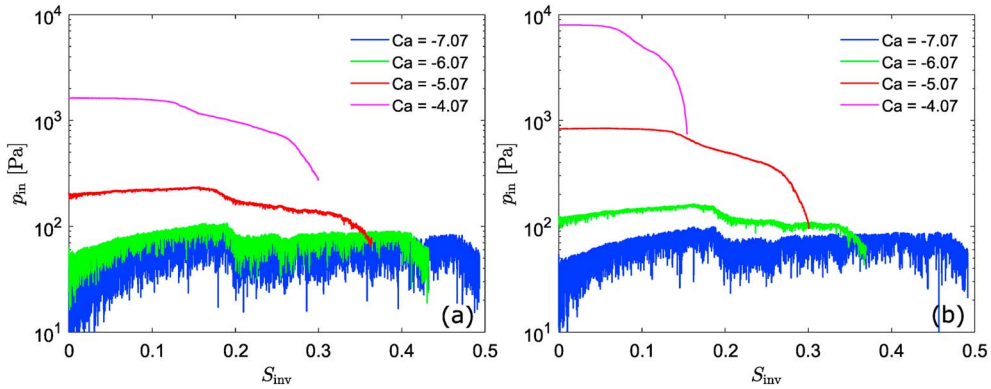

Figure 13. Evolution of inlet pressure with invading phase saturation viscosity ratios (a) $M = 1/100$ and (b) $M = 1/500$. The aperture field's standard deviation is 0.18 mm.

10.1029/2018WR024045

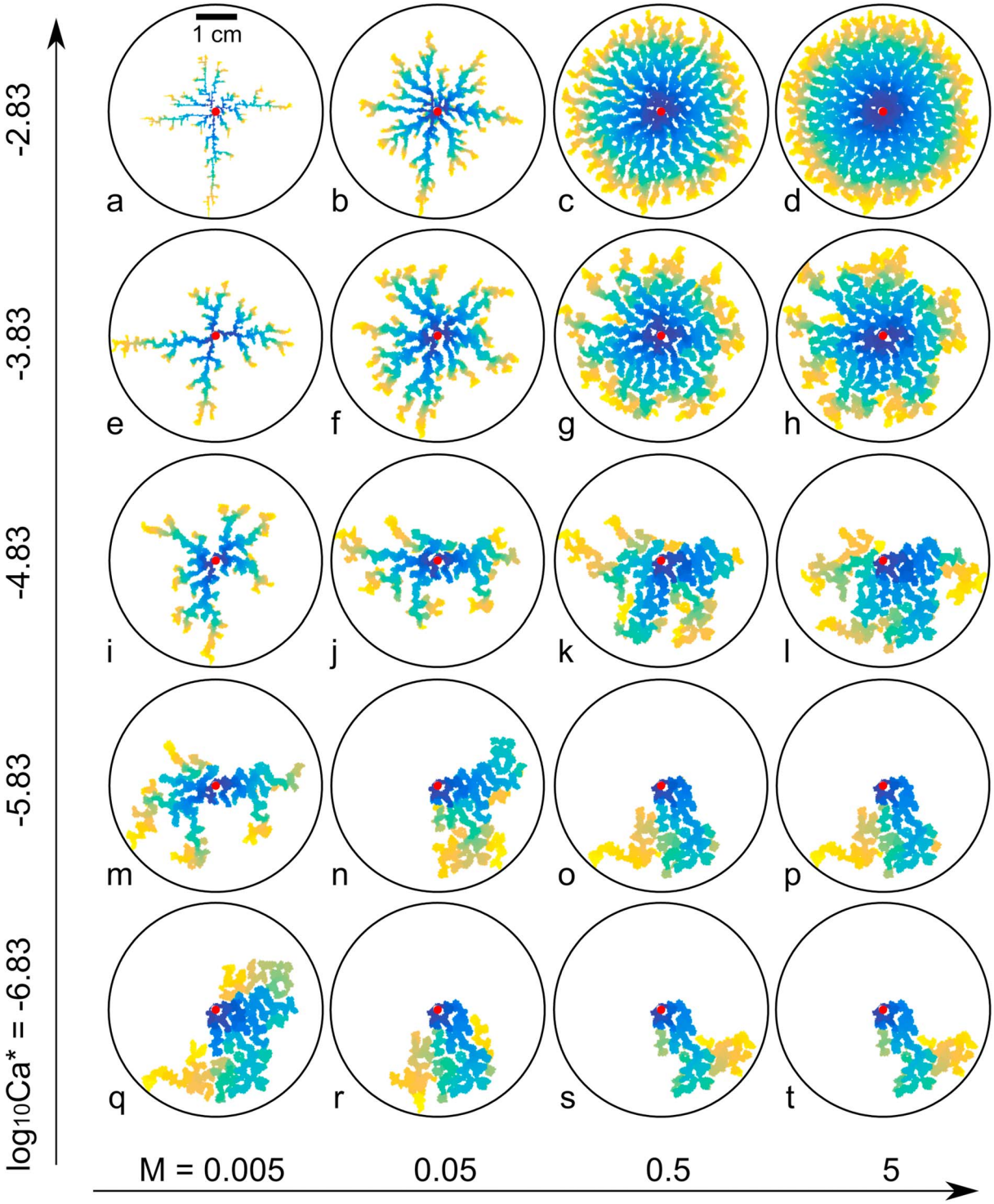

Figure 14. Immiscible displacement patterns at breakthrough for the radial injection scenario with contact angle = 0° (drainage). The injection rate increases from bottom to top for each column. (a, e, i, m, and q) the viscosity ratio $M = 0.005$; (b, f, j, n, and r) $M = 0.05$; (c, g, k, o, and s) $M = 0.5$;(d, h, l, p, and t) $M = 5$. Colors from blue to yellow represent invading times from early to late (breakthrough).

10.1029/2018WR024045

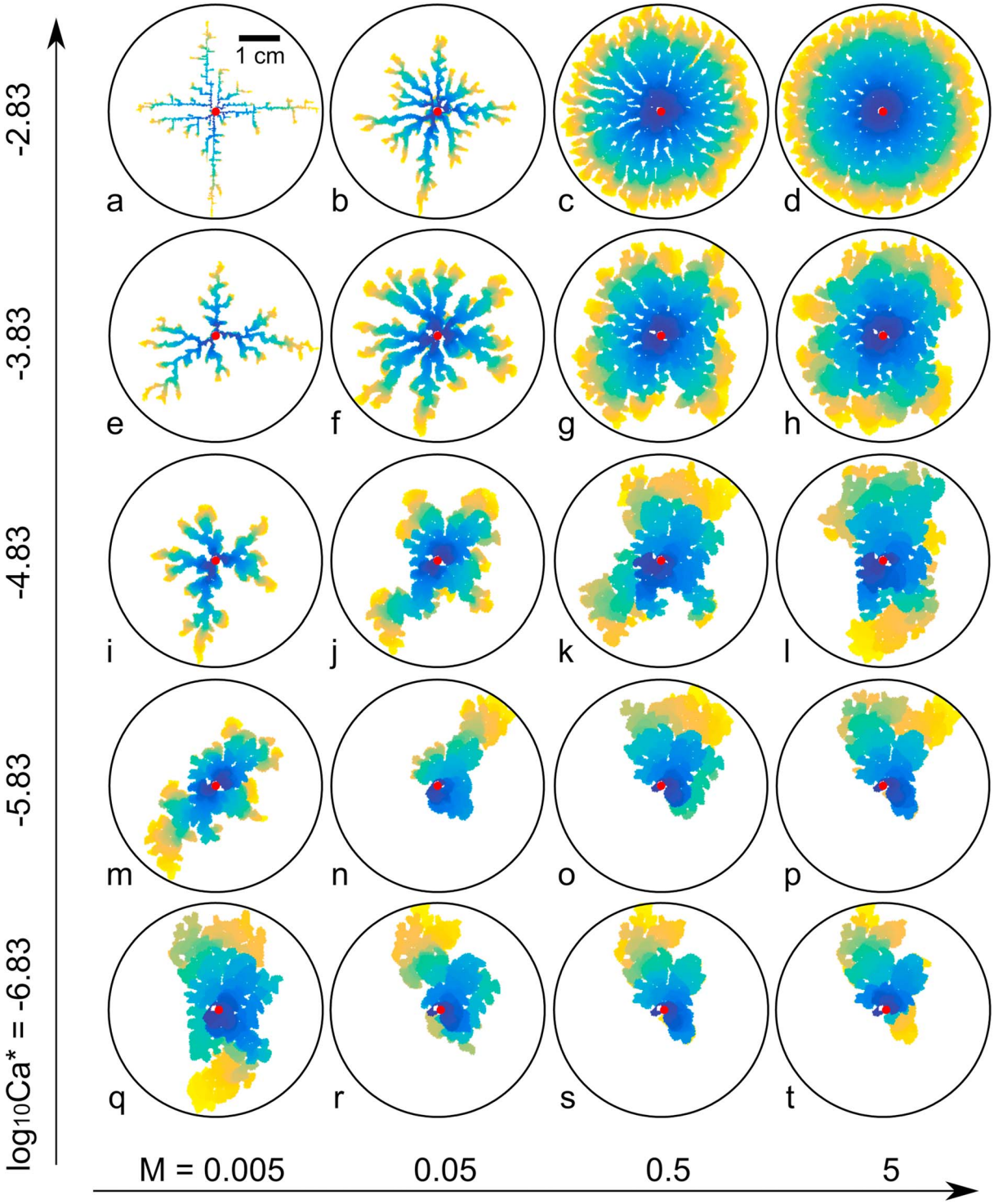

Figure 15. Immiscible displacement patterns at breakthrough for the radial injection scenario with contact angle = 60° (drainage). The injection rate increases from bottom to top for each column. (a, e, i, m, and q) the viscosity ratio $M = 0.005$; (b, f, j, n, and r) $M = 0.05$; (c, g, k, o, and s) $M = 0.5$;(d, h, l, p, and t) $M = 5$. Colors from blue to yellow represent invading times from early to late (breakthrough).

of the invading fluid at one edge with a fixed pressure value assigned to opposite edge, while other two edges were no-flow boundaries. In this scenario, the fluid-fluid displacement is forced to occur along a preset direction. But in many practical subsurface injection scenarios, the displacement occurs in a radial setting. Here, in addition to the scenario considered in the comparison and validation of the numerical model against experiments, we simulate immiscible displacement in a scenario where the injection happens at the center of the fracture domain. Since the flow diverges, a mean velocity cannot be calculated as in the parallel flow configuration addressed in section 3.2. Here, we define the capillary number Ca^* for the radial scenario as $\mathrm{Ca}^* = (\mu_{\mathrm{inv}} U_{\mathrm{inv}})/\gamma$ with the characteristic invading velocity $U_{\mathrm{inv}} = Q/(\pi R_0 \bar{b})$ where Q is the injection rate, R_0 is a characteristic length here taken to be half of the radius of the domain, and $\bar{b}$ is the mean aperture.

Figure 14 presents drainage patterns in the radial scenario simulated using different injection rates and viscosity ratios under strong drainage condition (zero contact angle). We observe that the invading pattern exhibits a higher degree of radial symmetry for larger capillary numbers. For the highest capillary number considered ($\log_{10}\mathrm{Ca}^* = -2.83$, top row), the invading pattern shifts from viscous fingering at small viscosity ratio ($M = 0.005$) to stable displacement at $M > 1$. For $M = 0.005$ (left column), the invading pattern gradually changes from viscous fingering to capillary fingering. For high capillary numbers, the pattern changes from fingering (viscous unstable) to compact (viscous stabilizing) with increasing M. In total, the model produces a visual phase diagram for the radial scenario in the Ca^*-M space, covering the three regimes of viscous-capillary flows.

Immiscible displacement patterns have been shown to be influenced by the wetting conditions (e.g., Dou et al., 2013; Holtzman & Segre, 2015; Hu et al., 2017a, 2017b; Jung et al., 2016; Trojer et al., 2015). Here, we have also simulated the displacement patterns under weak drainage condition (contact angle 60°), as shown in Figure 15. Again, the three regimes of stable displacement, viscous fingering, and capillary fingering can be observed. Compared with the pattern for the strong drainage condition (Figure 14), we see that generally, the invading phase is more compact in the weak drainage case. This behavior is due to the interface-smoothening effect of the in-plane curvature (Glass et al., 2003; Yang et al., 2016), which is analogous to the stabilization effect due to cooperative filling in porous media (Holtzman & Segre, 2015; Hu, Wan, et al., 2018; Trojer et al., 2015). In fact, the simulated patterns with the strong viscosity contrast ($M = 0.005$) for both the strong and weak drainage cases qualitatively resemble those observed in the experiment by Trojer et al. (2015) where $M = 0.003$.

4. Discussion

The key components of the numerical model presented here include (1) the calculation of the local capillary pressure jump according to the Young-Laplace equation and (2) the computation of the pressure field and its evolution as the interface advances based on mass balance and a quasi-steady assumption. We have shown that this model, albeit simple, is capable of simulating immiscible displacement patterns for a range of flow rates spanning over three orders of magnitude, and for immiscible fluids of arbitrary viscosity ratio. It is also capable of accounting properly for capillary pressure resulting from the in-plane curvature of the interface. It should be emphasized that the contribution of in-plane curvature to the local capillary pressure threshold is important in invading patterns, especially in the low capillary number regime (Yang et al., 2016).

It should also be pointed out that in this model film flow and corner flow are not accounted for. According to the experimental study by Zhao et al. (2016) on two-dimensional porous media consisting of cylindrical pillars, performed with a ratio of the defending fluid's viscosity to that of the injected fluid of ~340, film and corner flow occurs for strong imbibition (i.e., when the displacing fluid wets the solid surfaces sufficienly strongly) and this all the more as the capillary number is higher. The mechanism for this high velocity film flow has been demonstrated by Levaché and Bartolo (2014) in a Hele-Shaw geometry reminiscent of the Saffman-Taylor experiments (Saffman & Taylor, 1958); they show that the critical capillary number above which an interface instability leads to film flow decreases strongly when the viscosity ratio falls below 10^{-2}. On the other end of the Ca spectrum, both Lenormand (1990) in his seminal phase diagram for 2-D imbibition and Zhao et al. (2016) observe occurrence of film or corner flow at very low Ca under conditions of strong imbibition, in synthetic 2-D porous media. Thus, the present model is not expected to be suitable for predicting two-phase flow that involves sufficiently strong imbibition in particular at sufficienty large Ca, though for a fracture geometry, and depending on the viscosity ratio, the range of capillary numbers and

wetting angles for which our model still correctly predicts the physics at play may be rather significant in imbibition conditions as well. This remains to be investigated in detail. In any case the model is suitable for most drainage conditions. Drainage is a dominant process for NAPL migration in aquifers, a process which controls the contamination source zone characteristic, which is a critical issue in aquifer remediation. In geological sequestration, the injection and migration of CO_2 displaces the ambient brine, which is considered a drainage process for most rocks. In a leakage scenario, the displacement by CO_2 of the brine in a fracture within the caprock is also a drainage process.

The current model ignores the effect of gravity/buoyancy forces which may become important if the two fluids have a large density difference. This is rather simple to implement and will be the subject of later studies. Furthermore, assuming impermeable walls, the model does not consider fracture-matrix interaction which may alter the displacement dynamics. Given that typical matrix pore sizes are significantly smaller than fracture apertures, fracture-matrix interaction is mostly relevant for imbibition in fractured porous media (see, e.g., Arshadi et al., 2018; Kazmouz et al., 2016). In drainage configurations, the fluid-fluid interfaces are very unlikely to enter the matrix.

In the simulations against the experimental data, the model, when using the aperture field of the smaller standard deviation (0.12 mm), underestimates the amount of trapped defending fluid and in general results in more compact invading fluid structures than found in the experiments. When using the aperture field with the standard deviation of 0.18 mm, the simulations produce displacement patterns showing better resemblance to the experimental ones. These results thus demonstrate the role of aperture variation in controlling the fluid invasion patterns. Wettability can also influence the displacement dynamics. We find that decreasing the contact angle also leads to increased trapping and interface roughness (see Figure S3). As can also be seen in the simulations with radial geometry, the model would result in stronger trapping and less compact structures in different configurations. The focus is here, however, on the crossover from capillary to viscous fingering, which is well captured with the model when compared to the experiments.

It is also worth mentioning that the experiments conducted in Y.-F. Chen et al. (2017) considered even higher flow rates/capillary numbers. With the highest capillary number $\log_{10}\mathrm{Ca} = -3.07$, the displacement exhibited fingering patterns with branching and fragmentation of the invading fluid, producing blobs as the invading front advances (Y.-F. Chen et al., 2017, 2018). Such effects could be caused by locally high Reynolds numbers. For $\log_{10}\mathrm{Ca} = -3.07$, the superficial velocity $V \approx 0.25$ m/s, the Reynolds number $\mathrm{Re} = 2\langle b\rangle\rho_{\mathrm{inv}}V/\mu_{\mathrm{inv}} \approx 3.3 \times 10^2$; however, since the invading phase travels in thin fingers and does not occupy the entire cross-section area, the actual velocity of the invading fluid tips can be even higher, resulting in locally high Reynolds numbers manifesting the role of inertial forces which can promote formation of eddies and counterinvasion (i.e., situations where the defending phase displaces the invading phase). High flow rates can also lead to the increased pressure gradient within each phase which might lead to remobilization of trapped ganglia. The viscous pressure gradient (Δp) in the invading phase corresponding to the superficial velocity can be estimated as

$$\Delta p = 12\mu_{\mathrm{inv}}V/\langle b\rangle^2 = 12\mu_{\mathrm{inv}}Q/A\langle b\rangle^2, \tag{8}$$

where A is the inlet area. For $\log_{10}\mathrm{Ca} = -3.07$ ($Q = 100$ ml/s), Δp is approximately 696 Pa/m. For a trapped ganglion of 1 cm (which is a typical ganglion length), the viscous pressure drop through the invading phase is about 7 Pa, which is very small due to the low viscosity of the invading fluid. But, locally the viscous pressure drop can be larger, and thus can be comparable to the characteristic capillary pressure variation estimated to be $\frac{2\gamma\cos\theta}{\langle b\rangle}\frac{\sigma_b}{\langle b\rangle} = 20.1$ Pa, meaning that remobilization of trapped ganglia becomes possible. However, as Ca increases, trapping diminishes to nearly nothing: there are much less trapped ganglia and they become much smaller. Thus, the issue of trapped ganglia remobilization becomes much less significant. In the numerical model presented in this study, we do not take the counterinvasion process into account. Thus, the model is not expected to reproduce well the flow patterns at very high capillary numbers when the fragmentation mechanism has a big impact on the invasion pattern. However, we emphasize that the model is shown to faithfully capture the crossover from capillary dominated to viscous-dominated flows. Especially, the model can reliably deal with low capillary number flows. In contrast, capillary-dominated flows still present a major numerical challenge in the CFD approach with the widely used interface capturing methodologies, including volume of fluid method and Level Set method (Y.-F. Chen et al., 2018; Deshpande et al., 2012; Roman et al., 2016), due to the unphysical, spurious currents near the fluid-fluid interfaces resulting from lack of a discrete force balance and inaccurate calculation of interface curvature (Francois et al., 2006).

The strong advantage of the numerical model presented in this study is its computational efficiency over a three-dimensional (3-D) CFD approach such as that used by Y.-F. Chen et al. (2018), that is, an approach based on the resolution of the (Navier-)Stokes equations in the 3-D geometry. First, no discretization is needed in the z direction, which makes the numerical mesh much smaller. Second, the solution of (Navier-)Stokes equations is not involved, it is replaced by a Darcy law formulation that makes the numerically solution easy and efficient. In addition, in the planar direction, there is no need to use grid sizes much smaller than the mean aperture as the mean aperture sets a minimum length scale for the radius of in-plane curvature (Neuweiler et al., 2004). This makes the method much more efficient than even a (2+1)-D CFD approach (see, e.g., Ferrari & Lunati, 2013; Ferrari et al., 2015), where the Stokes equation is solved in 2-D with an additional force accounting for the friction of the top and bottom walls and a volume of fluid method to track the interface displacement. Here the simulations are all performed with serial computing, taking CPU time of a few hours, which can be further reduced without discernible loss of accuracy if we optimize the number of iterations and solutions of pressure distribution. Given the same scenarios ($M = 1/100$, $\log_{10}\mathrm{Ca} = -5.59$, -5.07, and -4.07), the full 3-D CFD approach of Y.-F. Chen et al. (2018) required tens of CPUs and took several days to even weeks (in the low capillary number displacements), resulting in computational times ranging between 5×10^3 and 5×10^4 core hours. Thus, the modeling approach presented here is at least 10^2 to 10^4 times faster than a full 3-D CFD model (and consequently, about 10 to 10^3 times faster than a (2+1)-D CFD model). In addition, the model is particularly efficient at large capillary numbers for which viscous pressure drops play an important role. Its computational efficiency decreases as the capillary number is decreased toward the capillary fingering regime, but in this regime the modeling approach can be easily reduced to a modified invasion percolation model by turning off the calculation of viscous pressure drops, in which case the computational time drops to just a few minutes or less.

5. Conclusions

We have developed a computational model capable of simulating emergent fluid invasion patterns in rough-walled fractures, governed by the interplay between capillary and viscous forces. This 2-D model takes into account the effect of capillary force on the fluid-fluid interfaces and viscous pressure drop in both fluid phases. The pressure distribution at each time step is solved based on mass balance and local cubic law, and an imposed pressure jump condition at the fluid-fluid interface according to the Young-Laplace equation, which includes both effects from the out-of-plane (aperture-spanning) curvature and the in-plane curvature. Characterization of the growth of invasion patterns in configurations that emulate viscous fingering drainage in 2-D random porous media shows that the effect of viscous forces is very well accounted for. Direct comparison with experimental results previously obtained in a rough fracture shows that the model can reproduce the observed patterns in terms of crossover behavior between capillary- and viscous-forces-dominated regimes. The evolutions of tip location and inlet pressure calculated from the model have been analyzed to characterize the transition from capillary fingering to viscous fingering regimes. In addition, a radial injection scenario of immiscible invasion has been simulated with varying modified capillary number and viscosity ratio to show the displacement patterns that fall into regimes whose dependence on the viscosity ratio and capillary number is similar to that of the classical phase diagram of Lenormand et al. (1988). Simulations in this radial configuration using two contact angles show that the invading phase becomes more compact when the wetting condition changes from strong to weak drainage. Future theoretic and modeling work is needed to systematically examine the important factors controlling the stabilization of the front during immiscible displacement in fractures.

This efficient, intermediate-scale model has been shown to capture the essential features of the capillary-viscous two-phase flow in rough-walled fractures, especially in drainage conditions. It is also expected to perform well in imbibition conditions for which corner or film flow do not significantly impact the invasion patterns. In contrast, pore-scale well-resolved two-phase flow CFD approaches, either 3-D or (2+1)-D require a much more significant amount of computational resources and are thus restrictive to address such studies at the relevant, mesoscopic, spatial scale. We therefore believe that this model can be used to bridge the gap in spatial scales between the full 3-D CFD modeling approaches and continuum Darcy-scale models. Future developments of the model will include accounting for the impact of density differences between the two fluids.

Acknowledgments
Financial supports from National Natural Science Foundation of China (41877203, 51779188, and 51579188) are gratefully acknowledged. The code for the simulations and data for tables and figures are available in the supporting information.

References

Amundsen, H., Wagner, G., Oxaal, U., Meakin, P., Feder, J., & Jøssang, T. (1999). Slow two-phase flow in artificial fractures: Experiments and simulations. *Water Resources Research*, *35*(9), 2619–2626.

Arshadi, M., Khishvand, M., Aghaei, A., Piri, M., & Al-Muntasheri, G. (2018). Pore-scale experimental investigation of two-phase flow through fractured porous media. *Water Resources Research*, *54*, 3602–3631. https://doi.org/10.1029/2018WR022540

Auradou, H. (2009). Influence of wall roughness on the geometrical, mechanical and transport properties of single fractures. *Journal of Physics D: Applied Physics*, *42*(21), 214015.

Basirat, F., Yang, Z., & Niemi, A. (2017). Pore-scale modeling of wettability effects on CO2–brine displacement during geological storage. *Advances in Water Resources*, *109*, 181–195.

Blunt, M. J. (2017). *Multiphase flow in permeable media: A pore-scale perspective*. Cambridge: Cambridge University Press.

Brown, S. R. (1995). Simple mathematical model of a rough fracture. *Journal of Geophysical Research*, *100*(B4), 5941–5952. https://doi.org/10.1029/94JB03262

Chandler, R., Koplik, J., Lerman, K., & Willemsen, J. F. (1982). Capillary displacement and percolation in porous media. *Journal of Fluid Mechanics*, *119*, 249–267.

Chen, Y.-F., Fang, S., Wu, D.-S., & Hu, R. (2017). Visualizing and quantifying the crossover from capillary fingering to viscous fingering in a rough fracture. *Water Resources Research*, *53*, 7756–7772. https://doi.org/10.1002/2017WR021051

Chen, Y.-F., Guo, N., Wu, D.-S., & Hu, R. (2018). Numerical investigation on immiscible displacement in 3D rough fracture: Comparison with experiments and the role of viscous and capillary forces. *Advances in Water Resources*, *118*(February), 39–48. https://doi.org/10.1016/j.advwatres.2018.05.016

Chen, C.-Y., & Horne, R. N. (2006). Two-phase flow in rough-walled fractures: Experiments and a flow structure model. *Water Resources Research*, *42*, W03430. https://doi.org/10.1029/2004WR003837

Deshpande, S. S., Anumolu, L., & Trujillo, M. F. (2012). Evaluating the performance of the two-phase flow solver interFoam. *Computational Science and Discovery*, *5*(1), 014016. https://doi.org/10.1088/1749-4699/5/1/014016

Detwiler, R. L., Pringle, S. E., & Glass, R. J. (1999). Measurement of fracture aperture fields using transmitted light: An evaluation of measurement errors and their influence on simulations of flow and transport through a single fracture. *Water Resources Research*, *35*(9), 2605–2617. https://doi.org/10.1029/1999WR900164

Detwiler, R. L., Rajaram, H., & Glass, R. J. (2009). Interphase mass transfer in variable aperture fractures: Controlling parameters and proposed constitutive relationships. *Water Resources Research*, *45*, W08436. https://doi.org/10.1029/2008WR007009

Dou, Z., Zhou, Z., & Sleep, B. (2013). Influence of wettability on interfacial area during immiscible liquid invasion into a 3D self-affine rough fracture: Lattice Boltzmann simulations. *Advances in Water Resources*, *61*, 1–11.

Edwards, R. W. J., Doster, F., Celia, M. A., & Bandilla, K. W. (2017). Numerical modeling of gas and water flow in shale gas formations with a focus on the fate of hydraulic fracturing fluid. *Environmental Science & Technology*, *51*, 13,779–13,787. https://doi.org/10.1021/acs.est.7b03270

Ferer, M., Crandall, D., Ahmadi, G., & Smith, D. H. (2011). Two-phase flow in a rough fracture: Experiment and modeling. *Physical Review E*, *84*(1), 016316.

Ferrari, A., Jimenez-Martinez, J., Le Borgne, T., Méheust, Y., & Lunati, I. (2015). Challenges in modeling unstable two-phase flow experiments in porous micromodels. *Water Resources Research*, *51*, 1381–1400. https://doi.org/10.1002/2014WR016384

Ferrari, A., & Lunati, I. (2013). Direct numerical simulations of interface dynamics to link capillary pressure and total surface energy. *Advances in Water Resources*, *57*, 19–31.

Fourar, M., Bories, S., Lenormand, R., & Persoff, P. (1993). Two-phase flow in smooth and rough fractures: Measurement and correlation by porous-medium and pipe flow models. *Water Resources Research*, *29*(11), 3699–3708. https://doi.org/10.1029/93WR01529

Francois, M. M., Cummins, S. J., Dendy, E. D., Kothe, D. B., Sicilian, J. M., & Williams, M. W. (2006). A balanced-force algorithm for continuous and sharp interfacial surface tension models within a volume tracking framework. *Journal of Computational Physics*, *213*(1), 141–173. https://doi.org/10.1016/j.jcp.2005.08.004

Glass, R. J., Nicholl, M. J., & Yarrington, L. (1998). A modified invasion percolation model for low-capillary number immiscible displacements in horizontal rough-walled fractures: Influence of local in-plane curvature. *Water Resources Research*, *34*(12), 3215–3234. https://doi.org/10.1029/98WR02224

Glass, R. J., Rajaram, H., & Detwiler, R. L. (2003). Immiscible displacements in rough-walled fractures: Competition between roughening by random aperture variations and smoothing by in-plane curvature. *Physical Review E*, *68*, 061110.

Holtzman, R., & Segre, E. (2015). Wettability stabilizes fluid invasion into porous media via nonlocal, cooperative pore filling. *Physical Review Letters*, *115*(16), 1–5. https://doi.org/10.1103/PhysRevLett.115.164501

Hu, R., Wan, J., Kim, Y., & Tokunaga, T. K. (2017a). Wettability effects on supercritical CO2-brine immiscible displacement during drainage: Pore-scale observation and 3D simulation. *International Journal of Greenhouse Gas Control*, *60*, 129–139. https://doi.org/10.1016/j.ijggc.2017.03.011

Hu, R., Wan, J., Kim, Y., & Tokunaga, T. K. (2017b). Wettability impact on supercritical CO2 capillary trapping: Pore-scale visualization and quantification. *Water Resources Research*, *53*, 6377–6394. https://doi.org/10.1002/2017WR020721

Hu, R., Wan, J., Yang, Z., Chen, Y.-F., & Tokunaga, T. (2018). Wettability and flow rate impacts on immiscible displacement: A theoretical model. *Geophysical Research Letters*, *45*, 3077–3086. https://doi.org/10.1002/2017GL076600

Hu, R., Wu, D.-S., Yang, Z., & Chen, Y.-F. (2018). Energy conversion reveals regime transition of imbibition in a rough fracture. *Geophysical Research Letters*, *45*, 8993–9002. https://doi.org/10.1029/2018GL079302

Huang, Z.-Q., Winterfeld, P. H., Xiong, Y., Wu, Y. S., & Yao, J. (2015). Parallel simulation of fully-coupled thermal-hydro-mechanical processes in CO2 leakage through fluid-driven fracture zones. *International Journal of Greenhouse Gas Control*, *34*, 39–51. https://doi.org/10.1016/j.ijggc.2014.12.012

Hughes, R. G., & Blunt, M. J. (2001). Network modeling of multiphase flow in fractures. *Advances in Water Resources*, *24*(3-4), 409–421. https://doi.org/10.1016/s0309-1708(00)00064-6

Huo, D., & Benson, S. M. (2016). Experimental investigation of stress-dependency of relative permeability in rock fractures. *Transport in Porous Media*, *113*(3), 567–590. https://doi.org/10.1007/s11242-016-0713-z

Jung, M., Brinkmann, M., Seemann, R., Hiller, T., & Herminghaus, S. (2016). Wettability controls slow immiscible displacement through local interfacial instabilities. *Physical Review Fluids*, *074202*, 1–19. https://doi.org/10.1103/PhysRevFluids.1.074202

Karpyn, Z. T., & Piri, M. (2007). Prediction of fluid occupancy in fractures using network modeling and X-ray microtomography. I: Data conditioning and model description. *Physical Review E*, *76*, 16315.

Kazmouz, S., Arshadi, M., Aghaei, A., & Piri, M. (2016). Micro-scale modeling of matrix-fracture interactions in fractured porous media. In *Paper presented at the International Symposium of the Society of Core Analysts, Snowmass, Colorado* (pp. SCA2016–090).

King, P. R. (1987). The fractal nature of viscous fingering in porous media. *Journal of Physics A: Mathematical and General*, *20*(8), L529.

Kneafsey, T. J., & Pruess, K. (1998). Laboratory experiments on heat-driven two-phase flows natural and artificial rock fractures. *Water Resources Research*, *34*(12), 3349–3367.

Kordilla, J., Noffz, T., Dentz, M., Geyer, T., & Tartakovsky, A. M. (2017). Effect of unsaturated flow modes on partitioning dynamics of gravity-driven flow at a simple fracture intersection: Laboratory study and three-dimensional smoothed particle hydrodynamics simulations. *Water Resources Research*, *53*, 9496–9518. https://doi.org/10.1002/2016WR020236

Lenormand, R. (1990). Liquids in porous media. *Journal of Physics: Condensed Matter*, *2*(S), SA79.

Lenormand, R., Touboul, E., & Zarcone, C. (1988). Numerical models and experiments on immiscible displacements in porous media. *Journal of Fluid Mechanics*, *189*, 165–187.

Levaché, B., & Bartolo, D. (2014). Revisiting the Saffman-Taylor experiment: Imbibition patterns and liquid-entrainment transitions. *Physical Review Letters*, *113*(4), 1–5. https://doi.org/10.1103/PhysRevLett.113.044501

Loggia, D., Bo, Z., Xiaorong, L., & Vasseur, G. (2009). Experimental study of upward oil migration in a fracture. *Transport in Porous Media*, *80*(1), 1–16.

Løvoll, G., Méheust, Y., Toussaint, R., Schmittbuhl, J., & Måløy, K. J. (2004). Growth activity during fingering in a porous Hele-Shaw cell. *Physical Review E*, *70*, 026301. https://doi.org/10.1103/PhysRevE.70.026301

Måløy, K. J., Feder, J., & Jøssang, T. (1985). Viscous fingering fractals in porous media. *Physical Review Letters*, *55*(24), 2688–2691.

Meakin, P., & Tartakovsky, A. M. (2009). Modeling and simulation of pore-scale multiphase fluid flow and reactive transport in fractured and porous media. *Reviews of Geophysics*, *47*, RG3002. https://doi.org/10.1029/2008RG000263

Méheust, Y., Løvoll, G., Måløy, K. J., & Schmittbuhl, J. (2002). Interface scaling in a two-dimensional porous medium under combined viscous, gravity and capillary effects. *Physical Review E*, *66*, 051603.

Murphy, J. R., & Thomson, N. R. (1993). Two-phase flow in a variable aperture fracture. *Water Resources Research*, *29*, 3453–3476. https://doi.org/10.1029/93WR01285

NRC (2005). *Contaminants in the subsurface: Source zone assessment and remediation* (344 pp.). Washington, DC: National Academies Press.

Neuweiler, I., Sorensen, I., & Kinzelbach, W. (2004). Experimental and theoretical investigations of drainage in horizontal rough-walled fractures with different correlation structures. *Advances in Water Resources*, *27*(12), 1217–1231. https://doi.org/10.1016/j.advwatres.2004.07.005

Nowamooz, A., Radilla, G., & Fourar, M. (2009). Non-Darcian two-phase flow in a transparent replica of a rough-walled rock fracture. *Water Resources Research*, *45*, W07406. https://doi.org/10.1029/2008WR007315

Persoff, P., & Pruess, K. (1995). Two-phase flow visualization and relative permeability measurement in natural rough-walled rock fractures. *Water Resources Research*, *31*(5), 1175–1186. https://doi.org/10.1029/95WR00171

Pyrak-Nolte, L. J., Helgeson, D., Haley, G. M., & Morris, J. W. (1992). Immiscible fluid flow in a fracture. In J. R. Tillerson, W. R. Wawersik, & A. A. Balkema (Eds.), *Rock mechanics. Proceedings of the 33rd US symposium* (pp. 571–578). Rotterdam, Netherlands: American Rock Mechanics Association.

Reitsma, S., & Kueper, B. H. (1994). Laboratory measurement of capillary pressure-saturation relationships in a rock fracture. *Water Resources Research*, *30*(4), 865–878. https://doi.org/10.1029/93WR03451

Roman, S., Soulaine, C., AlSaud, M. A., Kovscek, A., & Tchelepi, H. (2016). Particle velocimetry analysis of immiscible two-phase flow in micromodels. *Advances in Water Resources*, *95*, 199–211. https://doi.org/10.1016/j.advwatres.2015.08.015

Saffman, P. G., & Taylor, G. (1958). The penetration of a fluid into a porous medium or Hele-Shaw cell containing a more viscous liquid. *Proceedings of the Royal Society of London A: Mathematical, Physical and Engineering Sciences*, *245*(1242), 312–329. https://doi.org/10.1098/rspa.1958.0085

Su, G. W., Geller, J. T., Hunt, J. R., & Pruess, K. (2004). Small-scale features of gravity-driven flow in unsaturated fractures. *Vadose Zone Journal*, *3*(2), 592–601. https://doi.org/10.2113/3.2.592

Su, G. W., Geller, J. T., Pruess, K., & Hunt, J. R. (2001). Solute transport along preferential flow paths in unsaturated fractures. *Water Resources Research*, *37*(10), 2481–2491.

Tartakovsky, A. M., & Meakin, P. (2005). Simulation of unsaturated flow in complex fractures using smoothed particle hydrodynamics. *Vadose Zone Journal*, *4*(3), 848–855.

Tokan-Lawal, A., Prodanović, M., & Eichhubl, P. (2015). Investigating flow properties of partially cemented fractures in Travis Peak Formation using image-based pore-scale modeling. *Journal of Geophysical Research: Solid Earth*, *120*, 5453–5466. https://doi.org/10.1002/2015JB012045

Tokunaga, T. K., & Wan, J. (1997). Water film flow along fracture surfaces of porous rock. *Water Resources Research*, *33*(6), 1287–1295. https://doi.org/10.1029/97WR00473

Toussaint, R., Løvoll, G., Méheust, Y., Måløy, K. J., & Schmittbuhl, J. (2005). Influence of pore-scale disorder on viscous fingering during drainage. *Europhysics Letters*, *71*(4), 583–589. https://doi.org/10.1209/epl/i2005-10136-9

Toussaint, R., Måløy, K. J., Méheust, Y., Løvoll, G., Jankov, M., Schäfer, G., & Schmittbuhl, J. (2012). Two-phase flow: Structure, upscaling, and consequences for macroscopic transport properties. *Vadose Zone Journal*, *11*(3), vzj2011.0123.

Trojer, M., Szulczewski, M. L., & Juanes, R. (2015). Stabilizing fluid-fluid displacements in porous media through wettability alteration. *Physical Review Applied*, *3*(5), 1–8. https://doi.org/10.1103/PhysRevApplied.3.054008

Watanabe, N., Sakurai, K., Ishibashi, T., Ohsaki, Y., Tamagawa, T., Yagi, M., & Tsuchiya, N. (2015). New *v*-type relative permeability curves for two-phase flows through subsurface fractures. *Water Resources Research*, *51*, 2807–2824. https://doi.org/10.1002/2014WR016515

Wilkinson, D., & Willemsen, J. F. (1983). Invasion percolation: A new form of percolation theory. *Journal of Physics A: Mathematical and General*, *16*(14), 3365–3376.

Yang, Z., Neuweiler, I., Méheust, Y., Fagerlund, F., & Niemi, A. (2016). Fluid trapping during capillary displacement in fractures. *Advances in Water Resources*, *95*, 264–275. https://doi.org/10.1016/j.advwatres.2015.07.015

Yang, Z., Niemi, A., Fagerlund, F., & Illangasekare, T. (2012). A generalized approach for estimation of in-plane curvature in invasion percolation models for drainage in fractures. *Water Resources Research*, *48*, W09507. https://doi.org/10.1029/2012WR011829

Yang, Z., Niemi, A., Fagerlund, F., & Illangasekare, T. (2013). Two-phase flow in rough-walled fractures: Comparison of continuum and invasion-percolation models. *Water Resources Research*, *49*, 993–1002. https://doi.org/10.1002/wrcr.20111

Yang, Z., Niemi, A., Fagerlund, F., Illangasekare, T., & Detwiler, R. L. (2013). Dissolution of dense non-aqueous phase liquids in vertical fractures: Effect of finger residuals and dead-end pools. *Journal of Contaminant Hydrology*, *149*(0), 88–99. https://doi.org/10.1016/j.jconhyd.2013.03.006

Yeo, I. W., Ji, S.-H., & Lee, K.-K. (2003). Density-surfactant-motivated removal of dnapl trapped in dead-end fractures. *Geophysical Research Letters*, *30*(9), 1471. https://doi.org/10.1029/2003GL017186

Zhao, B., MacMinn, C. W., & Juanes, R. (2016). Wettability control on multiphase flow in patterned microfluidics. *Proceedings of the National Academy of Sciences*, *113*(37), 10,251–10,256. https://doi.org/10.1073/pnas.1603387113